Chemical Engineering Journal 499 (2024) 156212

Contents lists available at ScienceDirect

Chemical Engineering Journal

journal homepage: www.elsevier.com/locate/cej

Experimental and simulation-based engineering of calcium alginate self-healing asphalt capsules

Yujia Lu [a], Bingyan Cui [b], Hao Wang [b], Ramez Hajj [a,*]

[a] *Department of Civil and Environmental Engineering, University of Illinois at Urbana-Champaign, Urbana, 61801, IL, USA*
[b] *Department of Civil and Environmental Engineering, Rutgers, The State University of New Jersey, New Brunswick, 08854, NJ, USA*

ARTICLE INFO

Keywords:
Asphalt
Self-healing capsules
Inter-diffusion
Healing mechanism
Fine aggregate matrix
Molecular dynamics simulation

ABSTRACT

An emerging technology to mitigate the cracking of asphalt pavements is the use of self-healing capsules embedded in asphalt mixtures. In this study, self-healing capsules were fabricated by encapsulating asphalt rejuvenators with calcium alginate shells. While past studies have used a "brute force" design process for such capsules, the design and formulation of these can be optimized through careful consideration of chemical interactions and crack healing mechanisms. In this study, experiments and molecular dynamics (MD) simulation were used to engineer capsule–rejuvenator formulations to mitigate premature failure of capsules and improve self-healing efficiency. To explore the thermodynamic process, the inter-diffusion coefficient and blending degree between materials in the capsule system were evaluated at different temperatures and capsule designs to determine the ratio of capsules which survive mixing and compaction through molecular scale studies. MD provided an understanding of healing behavior by simulating and quantifying the fracture–healing–fracture process of the binder–capsule system. The experiments verified the MD model by quantifying oil release percentage from micro-extraction and recovery and fine aggregate matrix (FAM) healing efficiency. The research revealed that the interaction between asphalt binder, rejuvenator, and capsules highly depended on their chemical compositions and that the dose of capsule content influences the penetration degree, and structural failure process. Polymeric capsules experienced significant premature failure and content release at high temperatures (160 °C) compared to intermediate temperatures (25 °C) due to enhanced thermal movement. To optimize capsule performance, rejuvenators C and E, which had higher viscosities, required 30%–40% calcium alginate, while rejuvenator A with lower viscosity needed 40%–60% calcium alginate. Rejuvenators with more asphaltenes were more sensitive to the capsule shell protection effect, and strengthened healing efficiency, while rejuvenators with more aromatics resulted in better wetting and diffusion processes during healing. The healing index, derived from FAM experimental healing test and validated by simulations, indicated that approximately 40% shell material effectively prevented capsule breakage and resulted in a 50% reduction in healing capacity. This research therefore established a framework for engineering a combination of capsules for use at pavement scale based on an understanding of chemical interactions, mechanical properties, and experimental verification.

1. Introduction

Asphalt materials have been widely used in pavements due to their mechanical properties and high recyclability. One of the challenges of flexible pavements, which are pavements surfaced with asphalt mixtures, is aging because of volatilization, temperature, and ultraviolet light. Aged, or oxidized, asphalt is more brittle and stiffer, leading to a high potential for fatigue cracking [1,2] in pavements. In recent years, more than 90% of end-of-life asphalt pavements in the U.S. have been recycled [3]. The growing incorporation of reclaimed asphalt materials increases the concern for fatigue cracking due to their heavily oxidized nature [1,4].

Cracking nucleates and grows from microcracks, which accumulate into macrocracks under repeated loading. Early studies [5] evidenced and described fatigue by observing the drop in stiffness during the micro-damage stage. The reduction of the stiffness is attributed to the reduction of the bearing load area with the movement and breaking of molecules. Healing is the reversal process of cracking after a certain rest period [6]. Healing starts with the closure of the fracture surface, at which stage molecules start to interact across the crack surfaces

---

* Corresponding author.
E-mail address: rhajj@illinois.edu (R. Hajj).

https://doi.org/10.1016/j.cej.2024.156212
Received 18 June 2024; Received in revised form 30 August 2024; Accepted 26 September 2024

causing wetting of the cracked surfaces as a result of surface free energy [7]. Molecules then diffuse continuously until they randomize in the material, which has been validated using molecular dynamics (MD) simulation [8]. The wetting, diffusion, and randomization stages also result in the restoration of the strength of the material.

The intrinsic healing capacity is a function of material properties, aging levels, and temperature. When the healing capacity of aged samples is hindered, extrinsic healing approaches could be considered such as induction heating and self-healing capsules. Induction heating is utilized as a preventive maintenance approach but introduces aging potential. Healing capsule incorporation with rejuvenation is an option based on recent studies [9,10] which observed healing potential improvement for aged asphalt with the addition of rejuvenators. Calcium alginate capsules have been used in self-healing for many fields in the recent years, including water pipeline protection [11], medical hydrogel healing [12], and asphalt concrete self-healing [13–15]. Millimeter-sized calcium alginate capsules for asphalt were first proposed by Micaelo et al. [13] and explored by Al-Mansoori et al. [16] from perspectives of chemical and mechanical analysis. The calcium alginate capsule design has been applied and evaluated in dense graded mixes and stone matrix asphalt (SMA) [14,15]. Ruiz-Riancho et al. [14] found the fatigue resistance effect in SMA depended on the type of capsule design. Zhang et al. [15] applied the three point bending fracture–rest–fracture test on dense graded mixtures to evaluate the healing capacity. However, less attention has been drawn to understanding the healing process of encapsuled mixtures: capsule micro-cracking, healing agent release, diffusion, strength restoration, and the impact of capsule design on the healing process. In order to study the healing process, fine aggregate matrix (FAM), which is an asphalt mixture consisting only of the fine aggregate fraction and asphalt binder, has been widely used, as healing does not have a large impact from coarse aggregate. Kim et al. confirmed the consistency, cost-efficiency, and convenience of FAM by comparing the linear viscoelastic (LVE) behaviors, cracking, and permanent deformation features with that of full-size AC mixtures. Furthermore, Pavaldi et al. [17] observed that the damage and healing processes were generally concentrated in FAM. Therefore, FAM scale testing was used in the present study for experimental validation.

Although the design of capsules can be comprehensively evaluated by multiscale testing, the optimal material selections and dosages and corresponding mechanisms affecting these are not clear. For example, the healing effectiveness of rejuvenators could be associated with rejuvenator type. Grangeiro de Barros et al. [18] explained the higher healing potential of waste cooking oil compared to soybean oil could be attributed to the distinct diffusion rates of healing agents, encapsulated in the same calcium alginate capsule structure. However, the material-dependent diffusion mechanism was not investigated well due to limited experimental approaches and time required to do so.

In the recent years, MD has successfully facilitated the study of molecular-scale diffusion behavior [19] and mechanical property prediction and analysis [20], especially in bituminous materials. Bhasin et al. [21] developed binder healing models, measured intrinsic healing based on Wool and O'Connor's hypothesis [7], and evidenced the wetting behaviors of asphalt binder fractions. Entanglement of molecules with long but fewer branching chains contributed to the wetting process. Mechanical properties of materials have also been correlated with molecular interactions [22]. MD made quantitative analysis possible due to the predictable coordinates of all atoms without the employment of tracers [22,23]. MD also provided an understanding of the rejuvenator diffusion and molecular movement. Ren et al. [24] updated the aged binder structure in molecular simulation, and validated the diffusion between rejuvenators and aged asphalt by comparing simulations and rheological experiments. Yu et al. [25] observed the interactions between rejuvenators and aged binders. Rejuvenators mitigated aging of binders by dispersing their molecules around the asphaltenes and preventing the self-aggregation of asphaltenes. Although researchers have studied the effect of rejuvenators on improving binder properties, most simulated the rejuvenators using a simple and single-molecule structure. However, it is necessary to build unique rejuvenator models when studying the effect of different types of rejuvenators or demanding a more accurate modeling environment because the diffusion capacity of rejuvenation molecules depends on the structural characteristics of rejuvenators [26].

Also, the present capsule healing system consists of three phases of materials: asphalt binder, calcium alginate shell, and healing agent rejuvenators. The compositions of the three phases contribute to component interactions, thus affecting the damage and healing within the system. However, there have been few studies characterizing the molecular movement between capsule composite materials and thus healing efficiency of capsule shell materials with the incorporation of rejuvenators. The damage mechanism of the calcium alginate polymerized capsule is another critical problem in design because optimized capsules are expected to resist breaking during mixing and compaction [27] while releasing rejuvenators under traffic loading [28]. To be specific, during the production of asphalt mixtures, in the healing capsule, healing agents need to be covered by a calcium alginate shell sufficiently to avoid premature release. On the other hand, during traffic loading, capsules are designed to initiate fracture upon the propagation of cracking within asphalt. Also, the healing agent must diffuse into the damaged area and facilitate healing. The specific composition of materials therefore must be finalized based on chemical interactions under thermal movement and mechanical loading. Therefore, this study supports an understanding of chemical interactions by thermodynamic and mechanical simulations at the molecular scale.

2. Objectives

This study aimed to optimize the synthesis of calcium alginate self-healing capsules containing rejuvenators by investigating working mechanisms and validating these using experimental findings. Capsules were fine-tuned by balancing the proportion between calcium alginate and rejuvenators, and assessing different rejuvenator performances. Specifically, this study combined simulation and experiments from thermodynamics and mechanical perspectives to achieve two goals: (1) evaluate the capsule design effect on resisting oil release of capsules during self-healing asphalt materials production and (2) determine capsule design effect on self-healing efficiency.

3. Scope

Three types of rejuvenators were encapsulated in four different dosages of calcium alginate shell materials to explore the premature oil release behaviors. In the first step, the temperature effect on oil release was also evaluated to determine the optimum conditions to prevent oil release during mixing and compaction. The lowest required dosage of shell concentration was determined for each rejuvenator. Mechanical fracture of capsules as the result of binder crack propagation was simulated for determining the upper limit shell concentration for three capsule types and two dosages of calcium alginate. In this step, the three-phase systems (binder, calcium alginate shell, rejuvenators) were exposed to fracture, healing, and re-fracture to evaluate the healing capacity of each system.

From experiments, four asphalt mixture samples with different capsule designs and control asphalt mixtures without capsules were fabricated. The effect of rejuvenator type and calcium alginate dosage on the diffusion rate was captured by extracting and analyzing the diffused binders. The diffusion behavior was ranked and compared to verify the simulation results from the diffusion perspective. Mechanical healing tests based on the above-mentioned cylindrical FAM specimens were run to enable the identification of the healing efficiency of different capsule designs. The healing potential of each combination was also used to verify simulation results and present recommendations for future study.

4. Materials and experimental methodology

The asphalt binder used in the study was performance grade (PG) 64-22 binder, which is a commonly used asphalt binder in Illinois. Three types of rejuvenators were selected based on known chemical fractions from a previous study [29]. Rejuvenator A was a bio-oil, Rejuvenator C was a fatty acid derivative, and Rejuvenator E was a commercial modified vegetable oil. Each of these rejuvenators had known saturate, aromatic, resin, and asphaltene (SARA) content from the previous study. Raw materials to produce capsules included sodium alginate ($C_6H_7O_6Na$) purchased from Sigma-Aldrich and calcium chloride dihydrate ($CaCl_2 \cdot 2H_2O$).

4.1. Calcium alginate capsule fabrication and estimation of capsule composition

A visual summary of the procedure used for calcium alginate capsule fabrication is shown in Fig. 1. Water and rejuvenator were blended at an oil/water ratio (o/w) of 0.2. 100 mL rejuvenator was mixed with 500 mL water with a high shear mixer at 500 rpm. 15 g sodium alginate was added to the oil and water blend for 15 min at 25 °C to form a homogeneous solution. A 2% $CaCl_2$ solution was formed by adding 15.9 g calcium chloride dihydrate in 600 mL distilled water at 20 °C. 4% $CaCl_2$ solution and 30 g of sodium alginate were used for fabricating capsules with thicker layer of shell material as a comparison. The blended oil–water–alginate emulsion was then poured in a burette for dripping in $CaCl_2$ solution. The dripping rate was controlled to form separate droplets. The capsules were solidified in $CaCl_2$ solution based on the chemical reaction by Eq. (1). The capsules were washed under distilled water to remove remaining $CaCl_2$ solution on the surface. Washed capsules were dried under a fan for 48 h before storing them for later use. Capsules using rejuvenators A, C and E were prepared using the above-described methodology. These are referred to as Capsules 2 A, 2C, and 2E, respectively throughout the paper. In addition, a thicker capsule was fabricated using rejuvenator E with a double dose of shell material, referred to as 4E, for studying the capsule shell thickness effect.

In Fig. 1, environmental scanning electron microscopy (ESEM) images of a cross-section of a capsule demonstrates the porous nature of the fabricated capsules. The cavities formed by polymeric materials contained the rejuvenators, which served as the healing agents. The shell material percentage by weight of a dry capsule was estimated using the following methodology: according to the reaction shown in Eq. (1), in a solution of 100 g oil + 500 g water, NaAlg was the limiting reactant. The most calcium alginate generated was 13.82 g, which was 12.14% by weight shell material in a dry capsule. Although 0.5% was sufficient to react with NaAlg, the final calcium alginate product was closer to 12.14% by weight shell material, with more $CaCl_2$ involved in the reaction. This led previous researchers to modify the material strength by increasing $CaCl_2$ concentration up to 10%. However, it should be noted that calcium alginate could never reach higher than 12.14% no matter how much more $CaCl_2$ was added. However, when the original NaAlg and $CaCl_2$ concentration were doubled to be 5% and 4%, respectively, around 24.28% by weight of shell material would be created to cover the rejuvenator during production of Capsule 4E. Due to the uncertainty of shell thickness generation, the estimation of shell material was also considered in the simulation by comparing the trends of representative shell materials, such as 20%, 30%, 40% and 60% by weight of shell materials.

$$\mathrm{CaCl_2 + 2NaAlg \rightarrow Ca(Alg)_2 + 2NaCl} \qquad (1)$$

4.2. Self-healing fine aggregate mix fabrication and aging

Limestone aggregates with 2.36 mm Nominal Maximum Aggregate Size (NMAS) were batched with unmodified PG 64-22 binder (10% by weight) to form the FAM matrix. 1% of aggregates between the 1.18 mm and 2.36 mm sieve sizes were replaced by 1% capsules by weight in the mixes. Note that all capsules were between 1.5 and 2.0 mm in size. In order to avoid capsule breakage during mixing, capsules were added during the final 15 s of binder and aggregate mixing. Before compacting the mixtures, loose mixes were exposed to oven heating at 135 °C for two hours to simulate short term aging and exposed to 95 °C for three days to simulate long term aging based on the recommendations from NCHRP Project 9-54 [30]. The aged samples were compacted by a gyratory compactor to 80 mm by thickness and 150 mm by diameter to achieve 4% air voids. Compaction effort was adjusted for each sample in this step due to different mixture densities, since capsules replaced aggregates with different densities.

4.3. FAM coring, micro-extraction and recovery

Compacted cylindrical specimens were cored with a drilling machine to produce specimens with 20 mm diameter. The top and bottom parts were sawed to be 50 mm in height for later mechanical testing. The materials left by coring were utilized for extraction and recovery, which was used to check the oil release during production as described later in this paper. In the extraction and recovery step, because of the low quantity demand of testing materials using FTIR for oil release analysis, binder micro-extraction was employed. This procedure was proposed and verified by Filonzi et al. [31] to save operation time and cost. Note that to eliminate the effect of unbroken capsules on extraction, unbroken capsules were screened out as follows: 50 g asphalt materials were warmed for spreading, and unbroken capsules were then picked out from the spread mixes by a shovel manually, which was possible due to the low amount of material present. The screening procedure was conducted three times to separate capsules completely. Finally, 20 g of material from the screened mixtures were used for micro-extraction. Micro-extraction was conducted on the loose mixtures using toluene. The specific procedure is detailed in [31].

4.4. Oil release percentage based on fourier transform infrared spectroscopy

Note that biodegradation of calcium alginate can lead to the premature cracking of calcium alginate capsules. To address this concern, quantitative measurements were conducted to assess the impact of biodegradation, and the capsule design was refined to minimize premature breaking. Specifically, premature cracking was evaluated by measuring oil release using FTIR. In the inter-diffusion between healing agent layer and shell layer section of this paper, the healing content within capsules, combined with various thicknesses of calcium alginate, was assessed at different temperatures to examine the factors influencing premature failure.

The measurements were conducted using a Jasco FT/IR-4X FTIR spectrometer with an Attenuated Total Reflectance (ATR) module, recording spectra in reflective mode. Samples were preheated at 110 °C for 5 min to prepare them for testing and were then directly placed onto the FTIR stage using a spatula. All measurements were performed at room temperature (around 25 °C). Prior to each test, background spectra were collected to correct any background noise. The spectra were recorded from 400–4000 cm^{-1} with a resolution of 4 cm^{-1}, averaging 50 scans per measurement. Three replicates were recorded for each sample. The integration method was used to capture the area under the FTIR spectrum between the relevant bands of interest to compare the rejuvenator oil release after mixing and compacting. The extracted binders obtained after mixing and compacting were analyzed

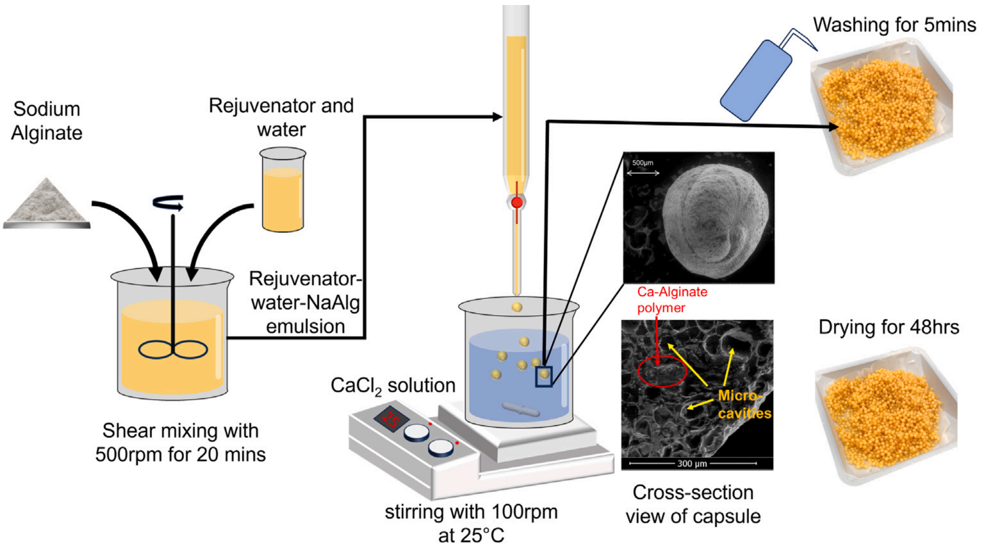

Fig. 1. Capsules fabrication procedure.

based on the carbonyl index (CI) (Eq. (2)) and sulphoxide index (SI) (Eq. (3)) from the FTIR spectra.

$$CI = A_{1745} / \sum A_{1325-1515} \tag{2}$$

$$SI = A_{1030} / \sum A_{1325-1515} \tag{3}$$

$$OR\% = \frac{A_{1745}}{A_{Rej+binder}} or \frac{A_{1030}}{A_{Rej+binder}} \tag{4}$$

where A_{1030} and A_{1745} refer the absorption areas concentrating on 1030 cm^{-1} and 1745 cm^{-1} of wavenumbers. $\sum A_{1325-1515}$ refers the area of the absorption peak of C–H bending, which changes less with aging.

The oil release calculation is based on Eq. (4). $A_{Rej+binder}$ is a referenced absorption area concentrating on 1745 cm^{-1} of mixed binder with a certain quantity of rejuvenators representing the homogeneously mixed oil and binder, which was therefore used to benchmark 100% oil release. For thin shell materials, the reference rejuvenator content was 7.36% by weight of binder, while for thick shell materials, the reference rejuvenator content was 4.72% by weight of binder (calculated using the estimation of capsule composition mentioned above).

4.5. *Experimental frequency sweep test*

FAM specimens were glued to the metal plates to be clamped on the machine for both frequency sweep and fatigue-healing tests. Linear viscoelastic characteristics were determined by the frequency sweep test with a 0.006% shear strain amplitude at frequencies ranging from 0.1 to 10 Hz in a dynamic shear rheometer (DSR) at 4 temperatures (15, 25, 35, 45 °C), shown in Fig. 2(a). The master curve was built with the sigmoidal function (Eq. (5)). Shift factors (a_T) were defined by the Williams–Landel–Ferry (WLF) [32] time–temperature superposition function (Eq. (6)). The test was also employed as a fingerprint test for specimens to calculate the damage rate parameter α, which is $1/m$ for stress-controlled tests, where m is the steady slope of the master curve. This parameter is used later in the viscoelastic continuum damage (VECD) analysis.

$$\log\left|E^*\right| = \delta + \frac{\alpha}{1 + e^{\beta+\gamma(\log f_r)}} \tag{5}$$

where $f_r = f - a_T$ represents reduced frequency, and α, β, γ are curve fitting coefficients.

$$\log a_T = \frac{C_1\left(T - T_0\right)}{C_2 + T - T_0} \tag{6}$$

where a_T is the shift factor for shifting data at temperature T to the reference temperature; C_1 and C_2 are fitting coefficients; T_0 is reference temperature (25 °C); and T is temperature at which data to be shifted were captured.

4.6. *Experimental fatigue and healing test*

Fatigue and healing tests were conducted at 25 °C, which is conventionally considered to be the intermediate temperature for PG 64-22 asphalt binder. During the healing test, the stress-controlled time sweep was applied to the FAM specimens until 20% reduction of the initial modulus. Tests were performed at 300 kPa stress amplitude and 10 Hz frequency. Four rest periods (40 min, 20 min, 10 min, and 5 min) were applied after each time sweep to determine the effect of the rest period on healing. After the rest period, the same specimen was utilized again until the same damage level. This single-specimen protocol was utilized in this study because the same specimen used for multiple rest periods could eliminate the effect of individual differences, and facilitate similar healing characteristics as multiple specimens applied with different rest periods [33]. Viscoelastic continuum damage (VECD) modeling was utilized to describe the damage propagation, which was consistent with other FAM studies on healing [17,33]. The VECD model represents the rate at which a material loses its integrity because of damage accumulation (Eqs. (7)–(9)) under repeated loading.

$$\gamma_P^R = \frac{1}{G^R}\left[\gamma^R \cdot |G^*|_{LVE}\right] \tag{7}$$

$$S(t) = S_0 + \sum \left[\frac{I}{2}(\gamma_P^R)^2(C_{i-1} - C_i)\right]^{\alpha/(1+\alpha)} \left[t_i - t_{i-1}\right]^{1/(1+\alpha)} \tag{8}$$

$$C(S) = \frac{G^R \cdot G_k^*}{|G^*|_{LVE}} \tag{9}$$

where γ_P^R is the pseudo-strain amplitude; γ^R is shear strain amplitude, $|G^*|_{LVE}$ is linear viscoelastic dynamic shear modulus; S_0 is the initial damage level, which is assumed as zero; α is the damage evolution rate, which is $1/m$ for a stress controlled test; C_i is pseudo-stiffness of each cycle; t_i is the time at each cycle; G^R is the constant in transformed space, which is treated as unity for simplicity; G^k is dynamic shear modulus of each cycle.

The healing index calculation determined by pseudo-stiffness might overestimate healing [10]. Also, pseudo-stiffness is not a material property as it depends on the test conditions [33]. To overcome these issues, the study utilized damage parameters before and after healing (S_b and

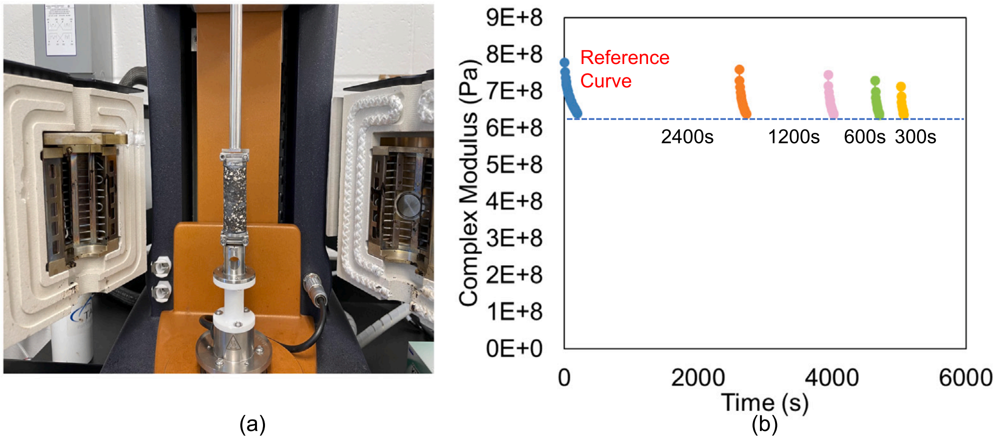

(a)

(b)

Fig. 2. (a) TA DSR machine with FAM mounted, and (b) Fatigue test protocol.

S_a) to define the healing index (HI) based on Eq. (10). The S parameters were obtained from damage characteristic curves according to t_b and t_a as shown in Fig. 2.

$$HI = \frac{S_b - S_a}{S_b} \times 100\% \tag{10}$$

where S_b refers damage parameter before healing, and S_a a refers damage parameter after healing

5. Molecular dynamic simulation procedure

Molecular dynamics simulation consisted of two parts: thermodynamic simulations and mechanical simulations. The thermodynamic simulations aimed at studying the effect of the concentration of polymeric shell materials on rejuvenator diffusion in capsules, which could be used to directly design capsules. Mechanical simulations were used to examine the effect of capsule design based on cracking susceptibility and healing efficiency on asphalt.

5.1. Material compositions and model development

Rejuvenators restore asphalt material properties by replenishing lighter fractions, broadly called maltenes. The diffusion between rejuvenators and binders due to similar hydrogen structures prevents agglomeration between molecules [34]. Previous researchers found rejuvenators share similar main components with asphalt [35,36]. Although the widely-used 12-component SARA fraction model developed by Li and Greenfield [37] provided reasonable results for most studies, oxidized functional groups were not considered in those structures. Recently, Ren et al. [24] developed molecule modification principles to modify the 12 fractions at different aging level based on the susceptibility to aging. Following the procedure described by Ren et al. [24], 12 component structures were modified to represent the different aging degrees, labeled with “0-4” at the end of the fractions shown in Fig. 3. 0 represents the original fraction, while 4 represents the most aged fractions with more oxidized molecules. In total, 21 fractions including original and aged fractions were matched with SARA fraction experimental results [29]. Therefore, the 21 established structures for rejuvenators and binders shown in Fig. 3 were employed in the present study.

Based on SARA fraction proportions obtained from [29], the number of each molecule in a given model was determined using Solver in Excel. The fractional distribution compared to experimental values was listed in Table 1. SARA weight percentages were compared with experimental results to verify the percentage in each fraction, as shown in Table 2. It should be noted that SARA fraction analysis can result in remaining residue during the first step of filtering samples due to existing insolubles. In order to enable the summation of four fraction percentages in the model to be 100%, the residue percentage is evenly distributed back to four fractions as a new percentage. The new percentage is labeled as corrected experiments in Table 2. Note that the modeling of insoluble fractions is outside the scope of the present study, but should be considered in future studies of rejuvenator modeling using MD.

Alginate is a copolymer originating from 1,4-linked-β-D-mannuronic (M) and α-L-guluronic (G) acids, as shown in Fig. 4(a) and (b). Based on the findings from [38,39], alginate can be formed as homopolymers (pure M blocks, G blocks), or copolymers (mixtures of M and G blocks) by various proportions of M and G units. The carboxyl group in G block binds preferentially with cations to form insoluble hydrogel [38], which is the shell material for capsules. The polymeric chain that consists of α-L-guluronic (G) and Ca was the focus of this study. The number of repeated units was selected based on the simulation scale. In this study, all rejuvenators were simulated with around 88 molecules in the simulation box. In this case, excessively long calcium alginate chains were avoided because the shell material requires a properly compacted height to be penetrated by rejuvenators for studying diffusion, while very short chains could not form a crosslinked structure for the purpose of mechanical simulation. Six repeated monomers were found effective in representing the G block in the simulation box. Throughout the study, the polymer length was also fixed to eliminate the effect caused by various unit numbers and better determine the concentration of calcium alginate polymers. The concentration of calcium alginate was achieved by varying the quantity of the polymer chain. The structure of calcium alginate was constructed in Materials Studio for facilitating the export to Large-scale Atomic/Molecular Massively Parallel Simulator (LAMMPS) [40] as shown in Fig. 4(c).

5.2. Part1: Inter-diffusion model between healing agents and capsule shell

All models in the study were first structured and pre-processed in BIOVIA Materials Studio. Consistent Valence Force (CVFF) force field [41] was utilized to cover non-bonded energy, such as Van der Waals, electrostatic interactions, and bonded energy, such as bond stretching, angle, dihedral, and improper torsional component. CVFF force field has been widely used to describe chemical interaction for asphalt [42], aggregates [43], and rejuvenators [44]. The total energy function of CVFF is described in Eqs. (11)–(13)

$$E_{total} = E_{bonded} + E_{nonbonded} \tag{11}$$

$$E_{non-bonded} = \sum_{VdW} 4\varepsilon \left[\left(\frac{\sigma_{ij}}{r_{ij}} \right)^{12} - \left(\frac{\sigma_{ij}}{r_{ij}} \right)^{6} \right] + \sum_{Ele} \frac{cq_i q_j}{\varepsilon_0 r_{ij}} \tag{12}$$

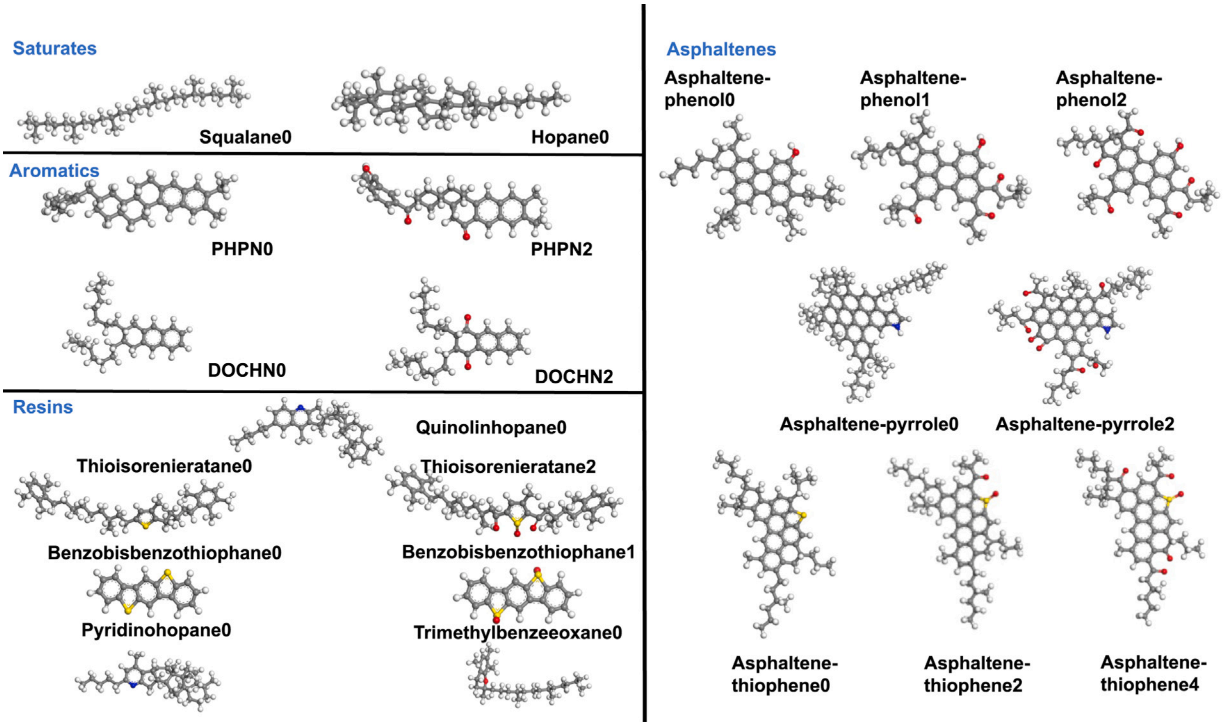

Fig. 3. Chemical structures of original and aged SARA fractions. (Structures ending with 0 represent the original form; Structures ending with 1, 2, 3, or 4 represent the aged form.)

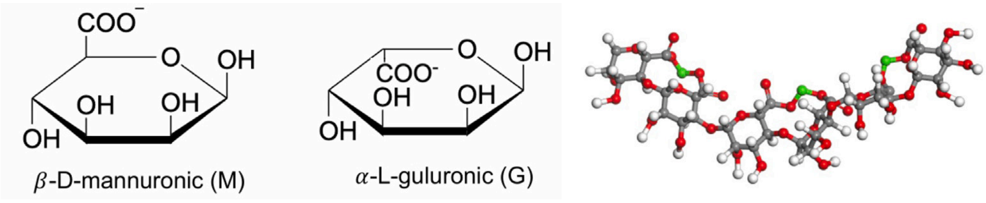

(a) (b) (c)

Fig. 4. Calcium alginate structures: (a) 1,4-linked-β-D-mannuroni (M) block, (b) α-L-guluronic (G) block, and (c) structure of calcium alginate in materials studio.

Table 1
Detailed SARA components for composing asphalt binder and rejuvenators.

Fraction		Chemical formula	E	C	A	PAV aged binder
Saturates	Squalane0	$C_{30}H_{62}$	0	1	4	6
	Hopane0	$C_{35}H_{62}$	0	0	5	8
Aromatic	PHPN0	$C_{35}H_{44}$	0	0	0	12
	PHPN2	$C_{35}H_{38}O_3$	0	0	10	0
	DOCHN0	$C_{30}H_{46}$	0	0	0	12
	DOCHN2	$C_{30}H_{42}O_2$	0	0	10	0
Resin	Quinolinohopane0	$C_{40}H_{59}N$	0	0	0	3
	Thioisorenieratane0	$C_{40}H_{60}S$	0	0	0	3
	Thioisorenieratane2	$C_{40}H_{56}SO_3$	0	0	50	0
	Benzobisbenzothiophene0	$C_{18}H_{10}S_2$	0	0	0	16
	Benzobisbenzothiophene1	$C_{18}H_{10}S_2O_2$	18	30	0	0
	Pyridinohopane0	$C_{36}H_{57}N$	0	0	5	4
	Trimethylbenzeneoxane0	$C_{29}H_{50}O$	61	45	1	2
Asphaltene	Asphaltene-phenol0	$C_{42}H_{54}O$	0	0	0	3
	Asphaltene-phenol1	$C_{42}H_{48}O_4$	0	3	0	0
	Asphaltene-phenol2	$C_{42}H_{44}O_6$	8	7	1	0
	Asphaltene-pyrrole0	$C_{66}H_{81}N$	0	0	0	1
	Asphaltene-pyrrole2	$C_{66}H_{67}NO_7$	0	0	2	0
	Asphaltene-thiophene0	$C_{51}H_{62}S$	0	0	0	3
	Asphaltene-thiophene2	$C_{51}H_{60}SO_2$	0	1	0	0
	Asphaltene-thiophene4	$C_{51}H_{54}SO_5$	0	1	0	0

Table 2
Experimental and simulation SARA composition comparison for Rejuvenators.

Rejuvenator	Weight (%)	Saturates	Aromatic	Resin	Asphaltene	Residue
A	Experiment	8.30	19.70	62.50	4.60	4.90
	Corrected experiment	8.70	20.70	65.72	4.84	–
	Model	8.73	20.70	65.73	4.80	–
C	Experiment	0.00	0.00	70.10	23.30	6.60
	Corrected experiment	0.00	0.00	75.05	24.94	–
	Model	0.04	0.00	75.05	24.90	–
E	Experiment	0.00	0.10	83.40	13.00	3.50
	Corrected experiment	0.00	0.10	86.72	13.27	–
	Model	0.00	0.10	86.42	13.47	–

$$E_{bonded} = \sum_{bond} K_r \left(r - r_0\right)^2 + \sum_{angle} K_\theta \left(\theta - \theta_0\right)^2 + \sum_{dihedral} K_n \times \left[1 + \cos(n\gamma - \gamma_0)\right] + \sum_{improper} K_\varphi \left[1 + d\cos\left(n\varphi_0\right)\right] \tag{13}$$

where ε, σ_{ij} are Lennard-Jones potential constants, r_{ij} is the distance between 2 atoms; c and ε_0 are coulomb constants; q_i and q_j are atoms charges. For bond energy, K_r, K_θ, K_n, and K_φ are bond strengthening, angle, dihedral, and improper constants, respectively; r is bond length; θ is bond angle, γ is dihedral angle, and φ is improper angle.

In the first simulation stage, as indicated by ESEM observation in Fig. 1, the healing agents and capsule shell polymer comprise the capsules. One goal of the present study was to optimize their relative proportions. Thus, a bi-layered system of rejuvenator and shell material was built to simulate the interaction between both materials. Hia et al. [45] also validated the shell wall-healing agent two layered compositions in the calcium alginate porous capsule. Based on the number of molecules in Table 1, the amorphous cell function was used for building a bulk rejuvenator layer at 298 K with a density of 0.6 $\mathrm{g/cm^3}$. The initial density parameters were selected based on two rules. The first rule was that the density should be below the estimated density—specifically, less than 1 $\mathrm{g/cm^3}$ for asphalt binder [37] and 0.9 $\mathrm{g/cm^3}$ for rejuvenators [46]—so that the model can be compacted to achieve equilibrium during simulation. The second rule was to optimize computational efficiency; if the initial density deviates too much from the estimated density, more time would be required to reach a stabilized state. A geometry optimization was run for 5000 iterations [47] to minimize system energy and optimize the 3-dimensional arrangement of atoms. An NPT ensemble (constant number of atoms, constant pressure, and constant temperature) was applied to the layer for relaxing and refining the structures for 80 ps under 1 atm pressure until when density and energy reached a steady state [23] as shown in Fig. 5. In order to match the dimensions in the x and y directions of the rejuvenator layer, the calcium alginate confined layer with four different percentages was constructed, respectively, but with the same length and width as the rejuvenator layer. All calcium alginate models were built with an initial density 0.6 $\mathrm{g/cm^3}$ for self-compaction during the relaxation process, following the same rationale mentioned previously. The thickness of the calcium alginate material layer was controlled by the number of calcium alginate structures. In the present study, the number of calcium alginate structures used was presented in Table 3. For example, the molecular mass of rejuvenator A is 49 862, while the molecular mass of a single calcium alginate chain is 1171.94. To build a Capsule A with 20%, 30%, 40%, and 60% capsule shell material, the number of calcium alginate molecules needed were therefore 11, 18, 28, and 64, respectively.

Two layers were then assembled with the build layer function. The bi-layered system was converted to an input data file for LAMMPS for inter-diffusion simulation. Energy minimization was conducted on the system for optimizing atom coordinates. For achieving the diffusion system along the z direction, reflective walls were established on two ends of the z directions. Periodic boundaries were established only in the x and y directions. The NPT ensemble was applied to the system for equilibrating the system to a stabilized density and energy for 1 ns at 298 K. Isothermal diffusion was then implemented on the system with NVT ensemble at 298 K and 433 K for 10 ns to simulate diffusion during the service life and mixing stage. A typical structure is shown in Fig. 13 at the start (0 ns) of diffusion and at 10 ns diffusion. For analyzing the simulation results, the density profile with time of each layer was recorded every 1000 steps, and averaged over 10 points of data acquisition. The mean square displacements (MSD) of each of the four SARA fractions of the rejuvenator layer were also measured and calculated with the same data acquisition frequency.

Table 3
Number of calcium alginate structures used in each model.

Shell materials content	Capsule A	Capsule C	Capsule E
20%	11	8	8
30%	18	13	13
40%	28	21	21
60%	64	47	47

5.3. Part 2: Rejuvenators, calcium alginate, and binder-three layered system model

A three-layered system was established to investigate the healing mechanism and calcium alginate impact on healing efficiency. To expose the system to horizontal tension, the x length of the box was extended by two times in the simulation. Correspondingly, the dosages of the rejuvenator and the shell material layers were doubled. Similar to the bi-layer system, three layers-rejuvenators, calcium alginate, and binder, were established and stabilized with energy minimization respectively. The three layers were then assembled using the build layer function. In this simulation, three rejuvenators were still utilized for observing different rejuvenator behaviors. 20% and 40% shell materials were built for studying the impact of shell thickness. In LAMMPS, a 1 ns NPT ensemble was applied first to relax and stabilize the simulated three-layer system.

To initiate cracking for the intact system, previous studies [9,48] established a vacuum pad to represent the gap between binders and rejuvenators, which might not accurately represent the capsule developed in this study. This is because the cracking failure surface might play a different role in promoting molecules forming new entanglements and bonds. Therefore, it is necessary to build an intact binder–capsule system for first damaging the system then healing the damaged system. Also, the damaged system served as a control to be compared with the recovered mechanical properties. Therefore, with the stable system, a 5 Å wide artificial notch with a length equal to the thickness of the binder was created in the system to facilitate the cracking propagation by deleting atoms and their compounds in the target area shown in Figs. 16 (a,e,i) and 17 (a,e,i). In order to evaluate the effect of shell materials and rejuvenator type on healing efficiency, 20%, and 40% shell materials for Capsule A, C, and E were generated by molecular mass proportions. To propagate the binder cracking into capsules, the system was then subjected to tensile loading with 10 m/s until 0.8 strain as a fixed damage level.

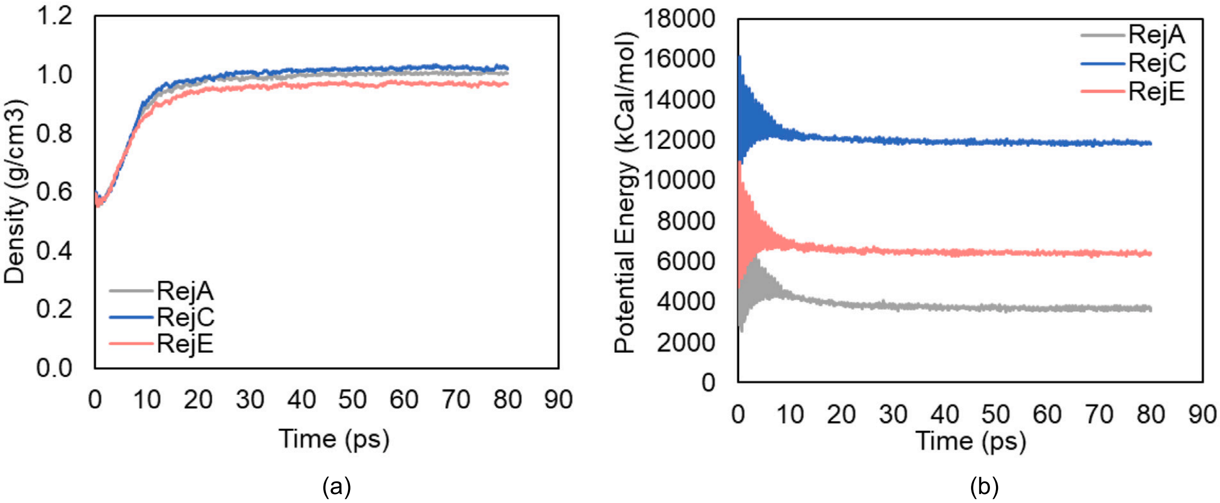

Fig. 5. (a) Density and (b) Potential energy of rejuvenators.

In terms of the healing process, previous studies showed the diffusion process dictated by NVT could facilitate healing [49]. This procedure was dominated by wetting and diffusion [50]. Less entanglement between molecules was established, but more realistic conditions were represented by existing confinement from boundaries. Therefore, healing simulations were also conducted with NPT ensemble [51], but diffusion impact from NVT condition might be underestimated. In the present study, to draw a more comprehensive conclusion, NVT assemblies were simulated for studying the wetting and diffusion effect on healing. Then the ambient pressure was applied in the next phase (NPT) after NVT diffusion to build more entanglement between binder and rejuvenator components. It should be noted that the simulation of NVT following by NPT might not be very realistic because in the field, the effects of constant volume and pressure confinement could happen simultaneously, even though wetting, diffusion, and entanglement take place sequentially. However, due to time-scale and length-scale limitations of MD, this was considered reasonable to make comparisons between materials in the present study. The cracked systems were healed with constant volume at 25 °C until potential energy reached equilibrium. To evaluate the healing effect, tensile strength was measured before healing, after NVT healing, and after the NPT healing stage.

6. Results and discussion

6.1. Experimental oil release

The viscosity of the three rejuvenators was measured to understand the relationship between oil release and material properties. The measurements were taken at 25 °C using a Brookfield rotational viscometer following the AASHTO T316-19 standard. The viscosities of rejuvenators A, C, and E were 40.4 cP, 135.8 cP, and 58.3 cP, respectively.

In terms of FTIR spectra, in Fig. 6, at wavenumber of 1030 cm^{-1}, the aged binder shows an obvious peak whereas the rejuvenator does not have a clear peak. Thus, the peak area around 1030 cm^{-1} for aged binder mixed with rejuvenator presents an almost overlapped area with aged binder area. This means S = O index is not the optimal parameter to detect the release of the rejuvenator. However, the carbonyl group around 1700 cm^{-1} for rejuvenator A was a better indicator for this study compared with the sulfoxide group, because the addition of rejuvenator A in aged binder results in an area between the region of aged binder, and the region of rejuvenator. The increased area was converted to the reference value in Eq. (4) because this region was assumed as the fully released oil case (100%). Therefore, the present study utilized CI based OR% to detect the oil release percentage.

Table 4
Capsule oil release.

Capsules	Thin A	Thin C	Thin E	Thick E
Oil release	42%	24%	33%	20%

As expected, aged binder showed the lowest C=O index whereas the samples with the addition of capsules showed a higher C=O index due to the oil release in Fig. 7. The capsule with thicker shells released less carbonyl fractions because fewer rejuvenator A fractions moved out of the capsules during mixing and compaction. Compared with the reference, each capsule had a unique oil release ratio, indicating that oil release depended on the healing agent used and the capsule design. In Table 4, with the same shell thickness, capsule A released the most oil during mixing and compacting. This indicated more drastic thermal movement happens to rejuvenator A than E and C. The reason could be the existence of more low polarity fractions such as saturates and aromatics in those capsules. It was observed that oil release and viscosity may be related to asphaltene content. Rejuvenator C, which has a higher asphaltene content, diffused more slowly than rejuvenator E, leading to lower oil release and higher viscosity. This suggests that rejuvenators with higher viscosity are less likely to release oil compared to those with lower viscosity. Also, the oil release from capsule E with different shell materials showed that capsules with double doses of shell raw materials could reduce oil release by 39.4%. Although the experiments provided a direct answer about the impact of shell thickness, the relationship between shell material percentage and oil release could be better understood and verified by thermal simulation, as shown below.

6.2. FAM characteristics and healing properties

Master curves were built to obtain the linear viscoelastic (LVE) fingerprint and the damage rate parameter α for each sample. From the curves in Fig. 8(a), samples with capsules showed stiffness lower than aged samples. In terms of healing effect, generally, a higher rest period results in a higher healing index as shown in Fig. 8(b), because the rest period allows the rejuvenator to diffuse into the cracked surfaces. For the effect of different capsules on healing, both rejuvenator type and shell material concentration play important roles. For all capsules with thinner shell materials, capsule A restored the aged asphalt to the highest level. This could be related to the highest oil release

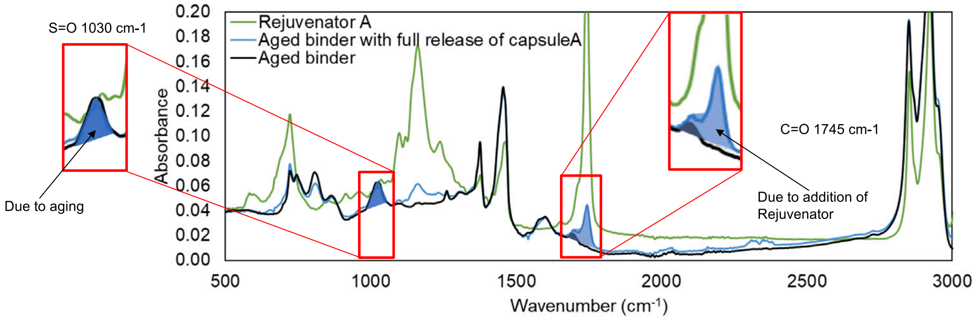

Fig. 6. FTIR spectrum areas of potential interest for oil release testing.

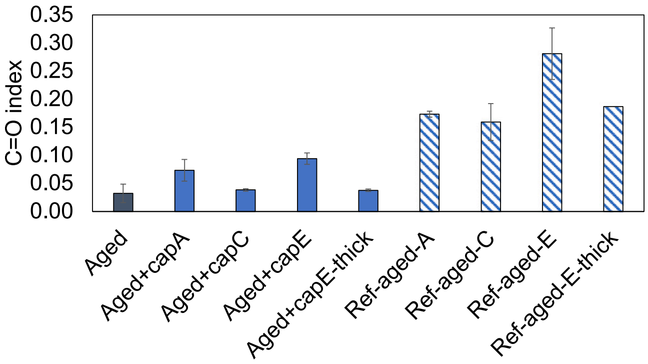

Fig. 7. Carbonyl index for extracted samples.

during mixing and compacting. Samples with capsule C perform better than E, for two potential reasons. One is that capsule E had more "wasted" oil during mixing and compaction based on Table 4; thus more rejuvenator remained in capsule C for activation during fatigue loading. The other reason could be that rejuvenator C contains more asphaltenes, which delay the release of rejuvenator until more damage is incurred, increasing the healing capacity. In terms of shell thickness, the capsules with thicker shells reduced the healing index by around 60% for all rest periods. This may be because the samples with more shell were less prone to rejuvenator release at this damage level.

6.3. Inter-diffusion between healing agent layer and shell layer

The temperature effects on the interaction between rejuvenators and shells were evaluated to understand the critical temperature impacting capsule integrity. Fig. 9 shows the movement of rejuvenators with 20% shell at 160 °C and 25 °C. Because the initial state before running diffusion was similar, density profiles at two temperatures at 1 ns were similar in Fig. 9. Slight differences may be due to temperature-dependent diffusion rate and average value acquisition within 1 ns. From Fig. 9 at 160 °C, the density in low concentration area increased with time, indicating that rejuvenators penetrated from the high concentration region to low concentration region (from rejuvenator area to shell layer area), which followed Fick's second law, which describes the relation between concentration, position, and diffusion time (Eq. (14)). Interdiffusion coefficient was selected to quantify the interaction between calcium alginate and rejuvenators because similar diffusion between asphalt and rejuvenators have been characterized by Sun and Wang [26] and Xu et al. [19] and validated to be on the same order of magnitude as experiments. However, it was hard to differentiate the similar density profile change rate for three rejuvenators at the low concentration region at 25 °C compared to that of 160 °C. This indicated that the interaction between rejuvenators and shell layers had more impact at a higher temperature mainly due to the increased kinetic energy [46]. Premature oil-release of capsules was prone to happening at high mixing and compaction temperatures. Therefore, in this study, the diffusion rate-related comparison, including the degree of blending analysis, critical healing agent, and shell material dosage selection focused on high-temperature behavior.

$$c(z,t) = c_0\left(1 - \mathrm{erf}\left(\frac{z}{2\sqrt{D_0 t}}\right)\right) \tag{14}$$

where $c(z,t)$ is the density function of z and t; z is the length along z-axis; erf is the error function; D_0 is the inter-diffusion coefficient; t is time.

Because the interest of the study was the comparison of the diffusion behavior of distinct percentages of calcium alginate shell material, the inter-diffusion rates of the shell layer for Capsule A, C, and E were derived and compared in Fig. 10. Diffusion rate decreases with shell dosage because the network of calcium alginate hinders diffusion of rejuvenators. The inter-diffusion rate calculated in Fig. 11(a) also indicated that with the same shell material in the capsules, rejuvenator A diffused faster than C and E, which might be due to the higher dosage of light-mass saturates and less heavy-mass asphaltenes in the chemical compositions. Also, A was the only rejuvenator containing saturates among the three rejuvenators. C and E both consisted of two groups: resins, and asphaltenes. However, the resin content in E was higher than that of C, resulting in faster diffusion.

Mean square displacement (MSD) has been commonly used to describe self-diffusion with time. Ghaffari and Rahbar-Kelishami [52] observed sodium and chloride ion diffusion in water and explained the effect of temperature using this parameter. This led us to use MSD parameter to understand diffusion of SARA fractions for rejuvenators A, C, and E. Fig. 12 illustrated the MSD curve as a function of time; the initial and final unstable stages were eliminated to describe traveled distance of SARA fractions compared to their initial positions. The slopes of the linear part of MSD for SARA fractions with various rejuvenator and calcium alginate combinations are compared in Table 5. MSD slopes showed a decreasing trend with calcium alginate for three rejuvenators, because the calcium alginate addition prevents molecular movement. In capsule A, saturates diffused more than resins, aromatics, and asphaltenes, because of the molecular weight differences. The trend was similar to previous asphalt binder observations [53]. However, for rejuvenators whose SARA fraction proportions were not necessarily similar, each fraction in SARA diffuses differently. For example, in capsule C with various calcium alginate dosages, the MSD slope of resins was higher than that of asphaltenes and saturates, which was the opposite trend compared to capsule A (Table 5). This indicated that diffusion of SARA depends on not only molecular weight but component concentration. Also, by the comparison of Table 5 with inter-diffusion rate shown in Fig. 11(a), although for the same rejuvenators, MSD slope decreased with increased concentration of calcium alginate, it was therefore difficult to obtain an index from MSD for discerning different rejuvenators. In conclusion, MSD slope cannot be

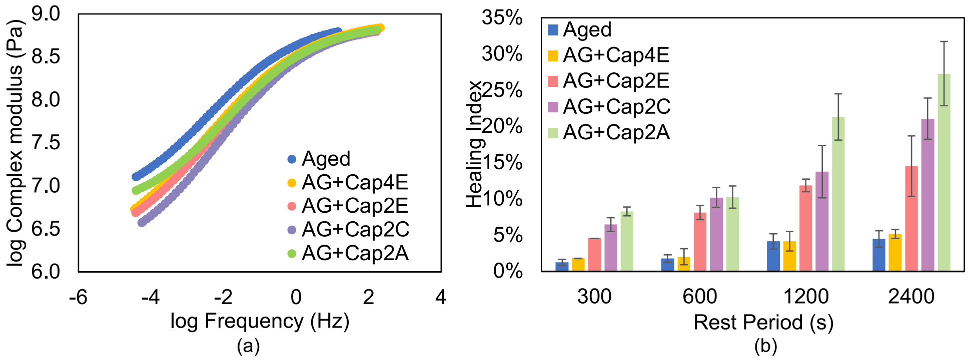

(a)

(b)

Fig. 8. Master curves (a) and healing index (b) from FAM for aged sample and aged sample with capsule A, C, and E.

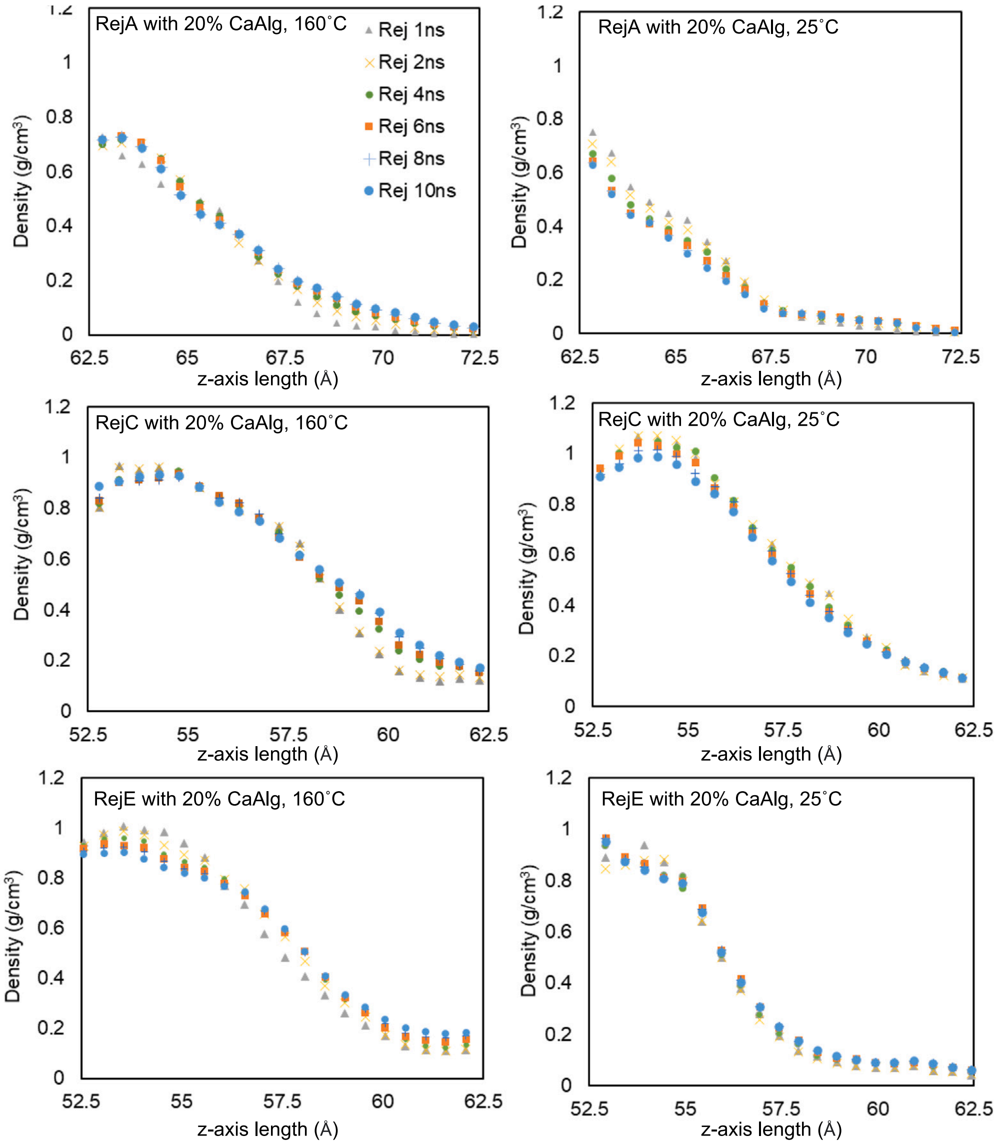

Fig. 9. Density profiles of rejuvenators with 20% of shell materials at 160 °C and 25 °C.

used to compare different rejuvenators, because the diffusion involves two layers, whereas MSD slope only describes self-diffusion.

In order to quantify the inter-diffusion between the shell layers and rejuvenator layers at each time step, degree of blending (DOB) [23] was introduced. The mass density profile of the shell and rejuvenator layers was built by collection of atoms in 0.5 Å height sections. Because the box dimension did not change with time due to the NVT assembly, the area below the mass density profile could refer the molecular mass in the region.

$$DOB_i = \frac{m_i}{M} \times 100\% \tag{15}$$

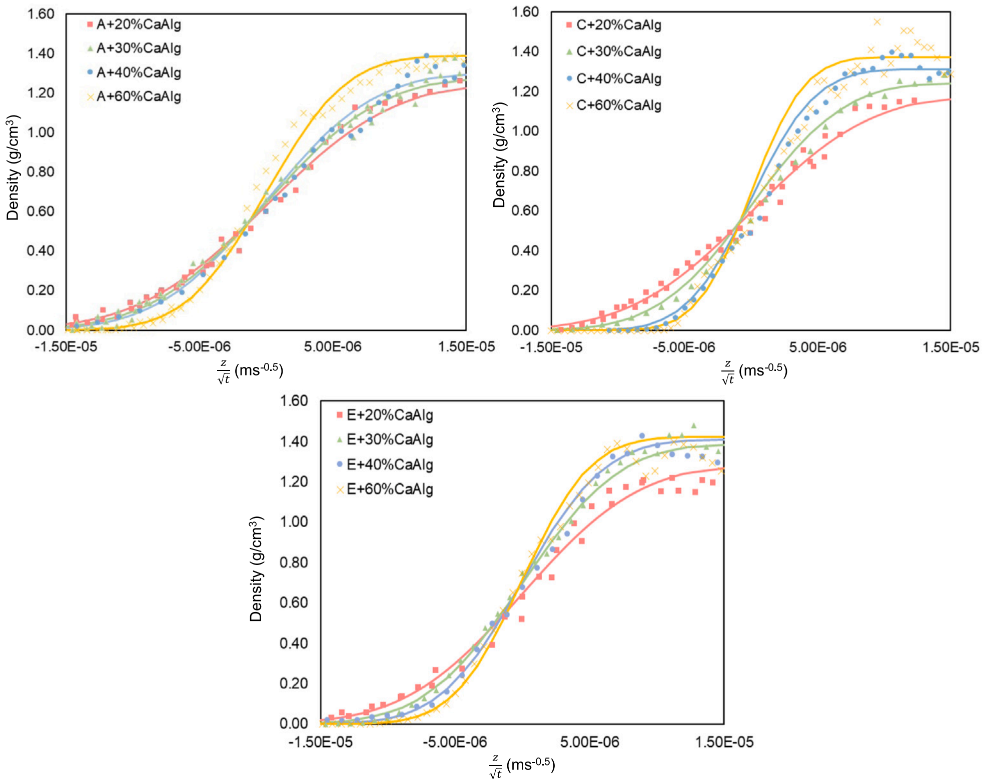

Fig. 10. Inter-diffusion coefficient fitting curves with 20%, 30%, 40%, and 60% of calcium alginate for capsule A, C, and E.

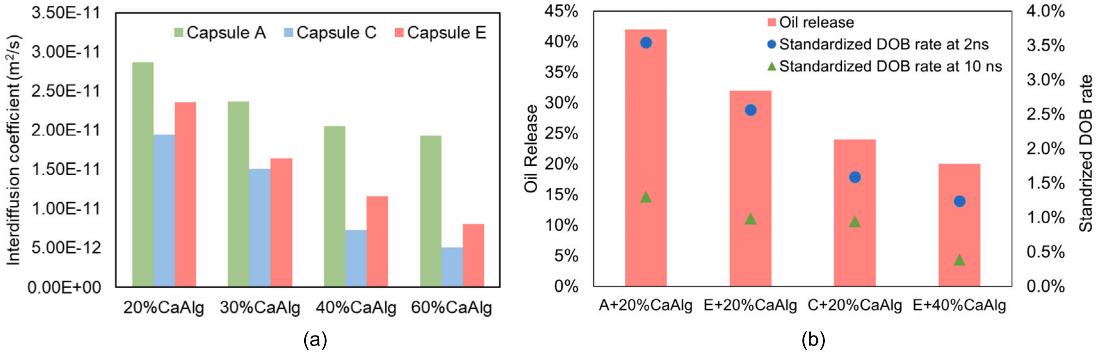

Fig. 11. (a) Inter-diffusion coefficients and (b) comparison between DOB rate and experimental oil release.

Table 5
MSD slope of SARA fractions for Capsule A, C, and E with various percentage calcium alginate.

	Saturates	R^2	Resins	R^2	Aromatics	R^2	Asphaltenes	R^2
A-20%calcium alginate	27.671	0.9017	16.451	0.9561	11.759	0.9811	7.8578	0.9326
A-30%calcium alginate	25.557	0.9448	11.571	0.9035	6.809	0.7699	4.1573	0.9398
A-40%calcium alginate	17.521	0.9303	7.8116	0.9655	6.1957	0.9426	3.4117	0.7297
A-60%calcium alginate	9.8438	0.9089	6.0331	0.947	4.0318	0.9317	2.5704	0.7954
C-20%calcium alginate	7.2249	0.7781	15.799	0.9149	–	–	9.3321	0.9358
C-30%calcium alginate	7.0423	0.882	14.969	0.9018	–	–	8.5795	0.91444
C-40%calcium alginate	4.112	0.7045	12.506	0.9574	–	–	6.4163	0.9136
C-60%calcium alginate	2.9886	0.7598	8.2528	0.9497	–	–	6.1288	0.9311
E-20%calcium alginate	–	–	28.497	0.9818	–	–	20.962	0.8701
E-30%calcium alginate	–	–	20.618	0.9533	–	–	14.693	0.9628
E-40%calcium alginate	–	–	20.602	0.9837	–	–	12.221	0.9412
E-60%calcium alginate	–	–	17.97	0.9531	–	–	7.81	0.8415

where m_i is the mass of calcium alginate in the blending area at time i and M is the total calcium alginate mass. DOB defined by Eq. (15) is illustrated in Fig. 13. Initially, the shell and rejuvenator layers were located at top and bottom ends of the box. As the rejuvenator phase moved towards the calcium alginate phase with time as shown in top simulation figures in Fig. 13, the density profile of rejuvenators

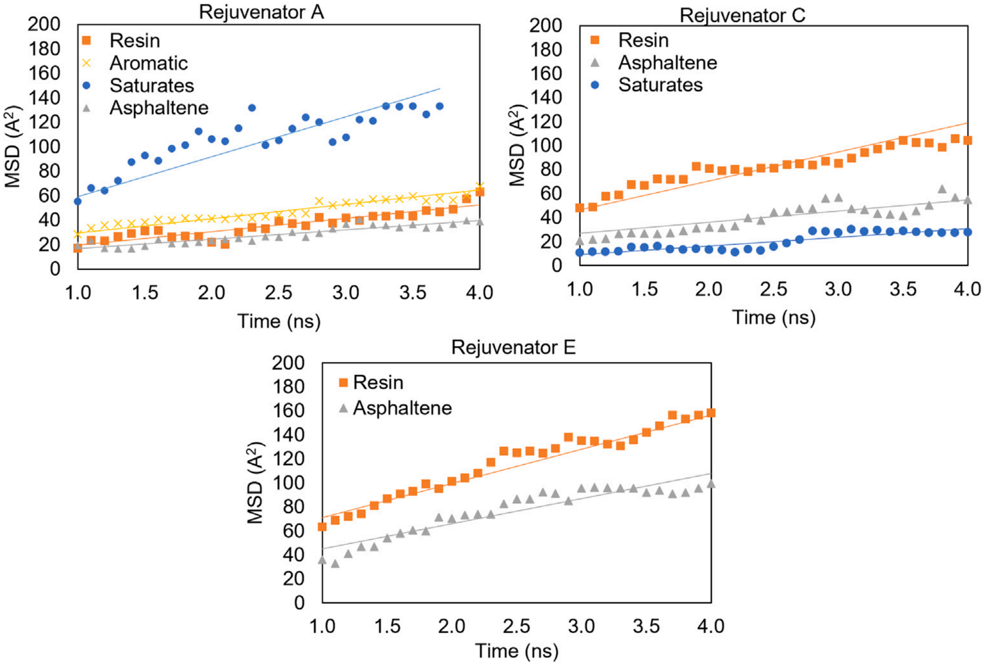

Fig. 12. MSD of SARA fractions of rejuvenator A, C, and E in the capsules with 20% calcium alginate.

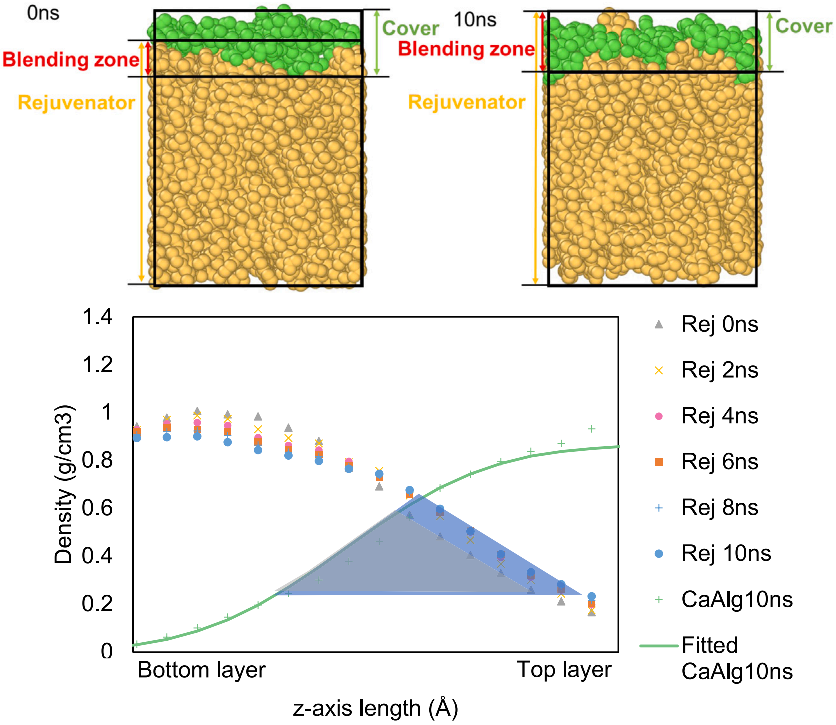

Fig. 13. Degree of blending (DOB) calculation.

decreased at the bottom of the box but increased at the top of the box due to diffusion. Thus, the Rej-Cover overlapped area shown in the profile diagram, referred to as the molecular mass in the blending zone, expanded from the gray area to the blue area with time, as shown in Fig. 13. The increased weight of the blending zone over the total weight represented the DOB.

In Fig. 14, degree of blending for rejuvenators A, C, and E decreased with calcium alginate percentages because the network formed by long chains of calcium alginate prevented movement of rejuvenators. Rejuvenator C is more susceptible to the addition of calcium alginate than A and E based on the reduction of DOB. This might be due to the high asphaltene content. The large molecules of asphaltenes are more likely to be trapped in the network of calcium alginate. Therefore, based on Fig. 14, the critical percentage of calcium alginate depends on rejuvenator type. Between 30% and 40% calcium alginate, there might be a critical point for capsule C and capsule E production to keep rejuvenators from releasing because the curves of DOB of almost reached a plateau with 40% calcium alginate. Meanwhile, capsule A

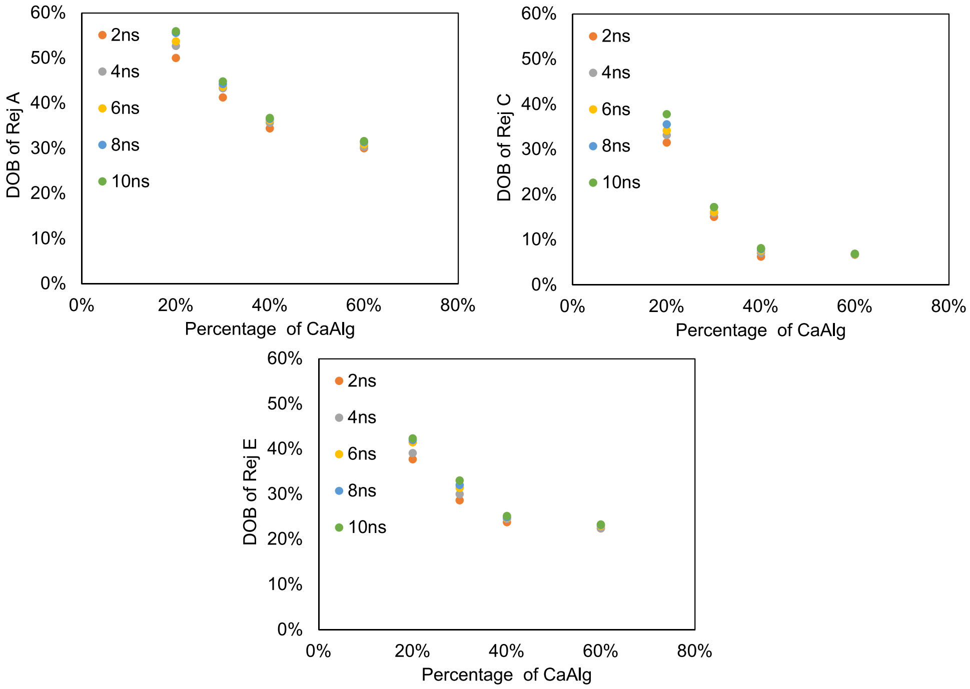

Fig. 14. DOB of capsules with rejuvenator A, C, and E with various calcium alginate.

might need 40% to 60% calcium alginate. Also the decreasing trend of band width of DOBs from 2 ns to 10 ns for all rejuvenators indicated that diffusion speeds decrease with calcium alginate. It should be noted that the initial DOB for these rejuvenator–calcium alginate combinations were different, so the standardization of DOB was necessary to compare the diffusion rate of rejuvenators.

The standardized rates of DOB showed the decreasing trend of diffusion with increased calcium alginate in Fig. 15. With different percentages of calcium alginate, all rates of DOB demonstrated rejuvenator diffusion rate of A is higher than E and C. Also, experimental results from oil release verified the simulation results from both inter-diffusion coefficient and rate of DOB aspects, which is demonstrated in Fig. 11(b), where with the same proportion of calcium alginate in the capsules, capsules with rejuvenator A diffuse more than E and C due to the SARA compositions as explained above. Here, experimental and simulation results were combined with chemical components and explained each other. Because the chemical compositions controlled the inter-diffusion of layers, the thermodynamic interactions between rejuvenators and calcium alginate finally caused the oil release. Moreover, simulation results provided insights into diffusion mechanisms. Rate of DOB revealed the diffusion rate is also a function of time. After a long diffusion time (10 ns in this case), all diffusion became slower than the initial state, so rejuvenators A, C, and E were not easily differentiated. However, the effect of doubled dosage of calcium alginate on preventing rejuvenator diffusion was still revealed compared to the thin shell layer.

6.4. Three layer system initial damaging, healing, and re-damaging simulation

In the three layer system, the initial loading fractured 20% calcium alginate as shown in Fig. 16 (b,f,j), whereas it could not cause complete fracture for the 40% calcium alginate structure (Fig. 17 (b,f,j)). Void formation and coalescence appear in the three rejuvenator layers labeled with red circles. This indicated that to activate the release of rejuvenators, larger fracture energy might be needed for the capsules with thicker shell material than capsules with thinner shell material.

In terms of healing of capsules with 20% calcium alginate, rejuvenators A, C, and E all diffused out of the calcium alginate to the openings in Fig. 16 (c,g,k). Specifically, the movement of rejuvenators were due to two different interactions in the simulation: diffusion due to concentration gradient shown with the straight arrows, and the intermolecular attractive forces by large-mass agglomeration at boundaries shown with the curled arrows. From the comparison of the three capsules, rejuvenator C was prone to being attracted by large-mass agglomeration at boundaries that dominated the interactions in the system, which might be due to the high percentage of asphaltenes. However, diffusion by gradient may dominate the interactions of rejuvenators A and E. As a comparison, although calcium alginate layers were not completely fractured for all three capsules in the case of the 40% calcium alginate system in Fig. 17 (c,g,k), rejuvenator A could still diffuse out of the calcium alginate while rejuvenator C and E remained in the capsules. This might be due to the high diffusion coefficients of rejuvenator A. That means the release of rejuvenators depends on both the original shell material dosage and the rejuvenator type. Rejuvenators C and E in capsules were not released after loading but voids formed during loading and were filled and compacted by rejuvenator self-diffusion as shown in Fig. 17(g,k). Also, it could be observed that rejuvenators C and E tended to move upward due to the concentration gradient as shown by the straight arrows. After NVT simulation, constant pressure and temperature were applied to the same systems until density of the systems reached equilibrium, where 200 ps were deemed enough for all systems. Entanglement of molecules between binder and rejuvenators, and between binders were observed after NPT, consistent with findings from a previous study [20]. Capsules with thin shells after NPT healed most of the artificial notch shown in Fig. 16(d,h,l). Capsules with thick shells (40% calcium alginate) could not effectively heal the gap in the current study, given the current specific damage level. This implied that capsules with thick shells could be activated when it comes to a higher damage level. Therefore, including capsules with different shell thicknesses in mixtures could be a better idea for practical applications, where distinct damage levels could take place at various locations. Then, weak capsules could heal the low-level damages while the stronger capsules would be saved for local high stress areas.

In addition to the first loading for crack propagation, three more tensile tests were applied to the system: before healing, after NVT,

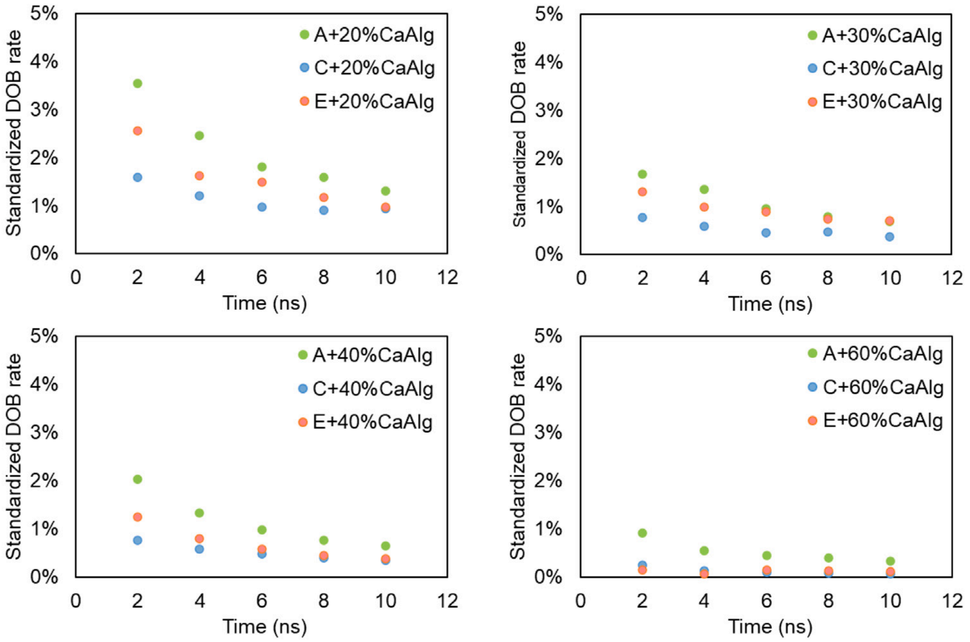

Fig. 15. Standardized DOB rate change with time for Capsule A, C, and E with various calcium alginate.

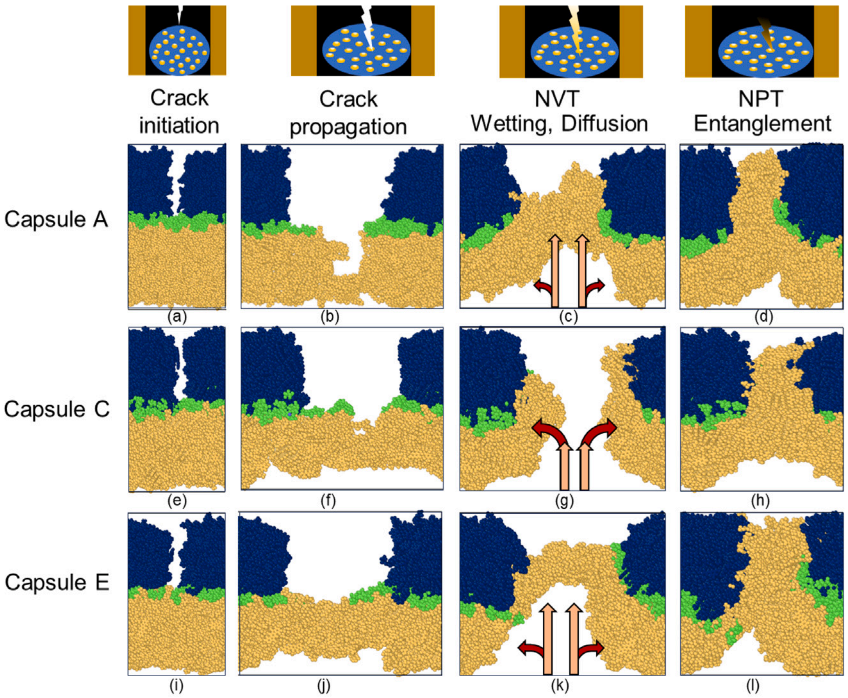

Fig. 16. Loading and healing process for capsule A, C, and E with 20% calcium alginate.

and after NPT to evaluate the recovered strength after different healing stages. The stress–strain curves measured by MD were shown in Fig. 18(a). Strain distribution in Fig. 18(b) showed that before healing, the tensile loading can easily rupture the system because the system has been damaged due to the initial loading. After NVT healing, the stress concentration from tensile loading happened to the contact point of two reconnected surfaces due to the weak connection during wetting, and diffusion. After NPT healing, tensile loading caused a more evenly distributed strain because entanglement during NPT restored the material integrity. Also, it could be observed from Fig. 18 that material ductility improves with wetting, diffusion, and entanglement. Failed material after NPT still showed stretched fibers, similar to a binder failure surface.

Fig. 19 shows the healing index based on the strength after NVT and NPT healing compared to the state before healing by Eq. (16). After NVT healing shown in Fig. 19(a), strength could be restored partially. Capsule A restored more than capsule E because of the higher diffusion rate of rejuvenator A. However, capsule C was not able to heal the system because the rejuvenator moved towards the binder surface instead of bridging the connection between the two failure surfaces.

$$HI = (S_a - S_b)/S_b \times 100\% \tag{16}$$

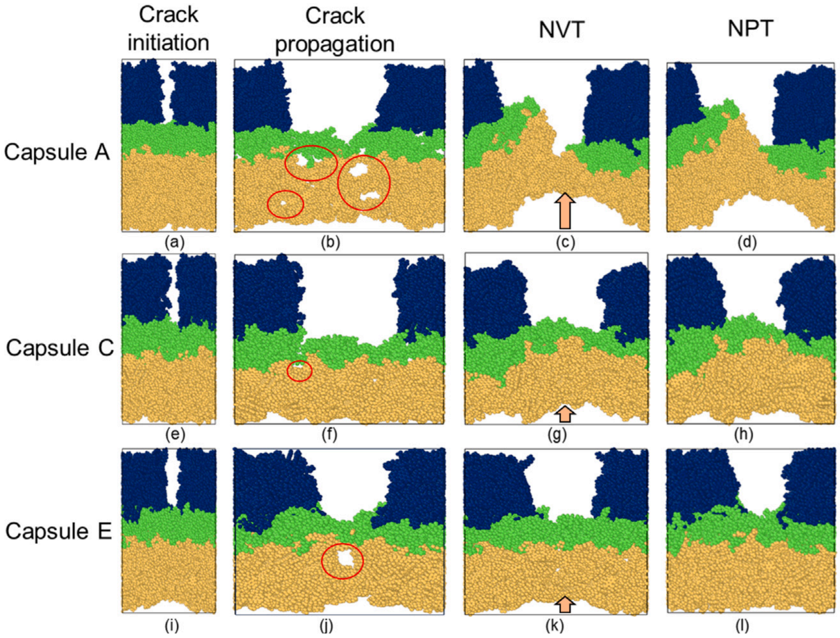

Fig. 17. Loading and healing process for capsule A, C, and E with 40% calcium alginate.

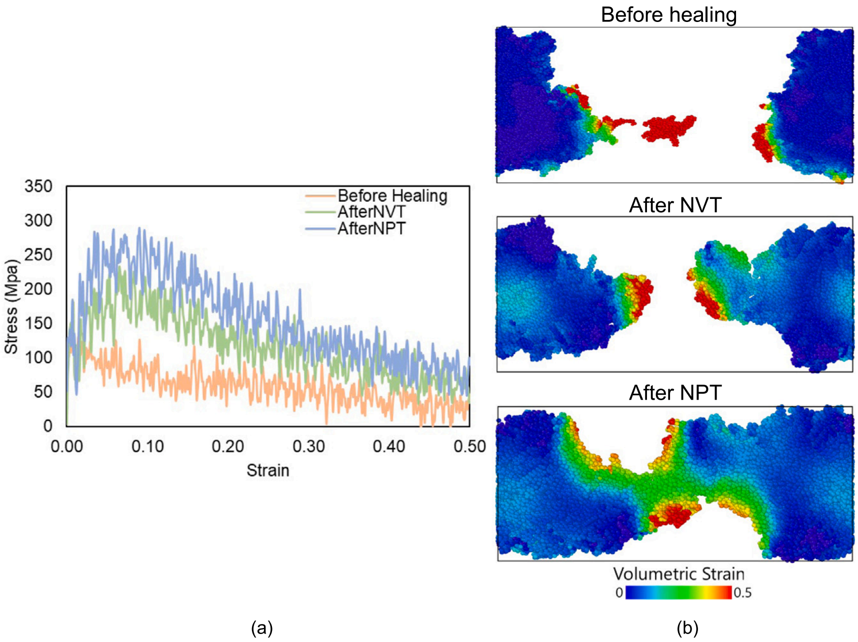

Fig. 18. Tensile tests before healing, after NVT, and after NPT for capsule A with 20% calcium alginate:(a) stress–strain curves and (b) strain distribution map.

where and S_a refers strength after healing, and S_b refers strength before healing.

Compared to NVT, the HIs after NPT healing in Fig. 19(b) were increased significantly; the trends of capsules A, C, and E correlate well with HI from experimental FAM tests in Fig. 8(b). The difference is HI between capsule E with 40% shell was 54% lower than that with 20% shell, while from experiments, the difference between these two different shell-coated capsules (E) was 60%–74%, depending on rest period length. A possible reason MSD was slightly lower might be that NVT and NPT process were established sequentially until the system reached equilibrium. The entanglement effect was amplified because diffusion and the confinement by the boundary materials in the realistic condition could happen simultaneously instead of sequentially. Also, macro-level material defects could prevent material property restoration while molecular simulation is still considered a nano-scale simulation. It should also be noted that simulation reflected the representative shell concentration effect, but the chemical reaction in experiments might include various concentrations of shell materials within the aforementioned estimated range for two types of shell thickness. In summary, the mechanical simulation ranked the capsules' effect on healing degree and the corresponding healing mechanisms but the values will differ from experiments, and therefore can be used for a quantitative ranking, but not precise prediction of experimental results.

6.5. Combined analysis of thermodynamics and mechanics

The study of interdiffusion and DOB rate provided insights into why rejuvenation capsule A was more prone to damage before application

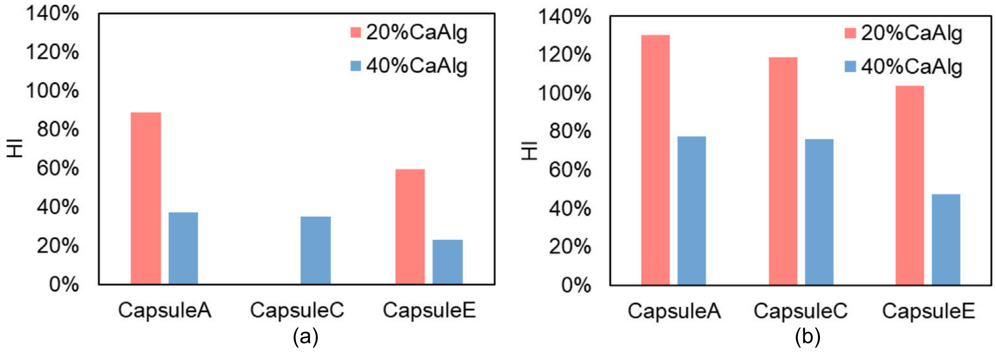

Fig. 19. HI after NVT (a), and after NPT (b) for capsule A, C, E with 20% and 40% calcium alginate.

compared to capsules C and E. This is the result of the molecular interaction between the chemical components. To prevent premature oil release, rejuvenators C and E required 30%–40% calcium alginate, while rejuvenator A needed 40%–60% calcium alginate. By mechanical simulation and evaluation, 40% calcium alginate could release rejuvenator A, but it would not lead to efficient out-diffusion for rejuvenator C and E in the three layer system. The recovered strength using capsule C and E with 40% calcium alginate was mainly contributed to by asphalt intrinsic healing instead of extrinsic healing. Therefore, the analysis from thermodynamics and mechanics suggests that rejuvenator A might need 40%–60% calcium alginate, while rejuvenator C and E might need 30%–40% calcium alginate. Specific dosages could be suggested in the future by further fine-tuning the simulations presented in this paper.

It is important to note that for field application, stress states in asphalt pavement are complex and unevenly distributed due to factors such as loading position, arrangement of aggregates, and loading amplitude. As a result, it is challenging to precisely control the release time and rate of capsules in all scenarios. This study highlighted the concept of using various capsule designs to accommodate the diverse stress states encountered in pavements. For instance, capsules with thinner shells may be more suitable for areas experiencing lower stress, where they can release their contents, while those with thicker shells remain intact until subjected to higher stress levels. Additionally, while materials with faster release times may improve healing efficiency, their susceptibility to premature breakage should be carefully considered.

7. Summary and conclusions

In this study, molecular dynamics simulation was used to assess the designs of encapsulated rejuvenators utilized in asphalt pavement for self-healing. Techniques for assessing healing potential were proposed based on the understanding of healing working mechanisms from simulations and corresponding experiments. 21 molecular structures were adopted in MD to describe the SARA fractions obtained from experiments in previous studies. In the thermodynamic simulation portion of the study, three rejuvenators were coated with four different thicknesses of polymeric materials to investigate and verify oil release obtained from FTIR during the fabrication stage. In the mechanical simulation portion, the three rejuvenators coated with 20% and 40% calcium alginate shells were simulated for understanding fracture and healing behaviors observed from FAM healing experiments. The following conclusions were obtained based on the main findings:

1. It was confirmed that FTIR could be utilized to detect rejuvenator release by chemical interaction during the mixing and compaction stage of fabricating self-healing asphalt. The effect of shell thickness was observed to have an important impact. Oil release could decrease by 39% by doubling the amount of shell material used to encapsulate rejuvenators.
2. The macro-level capsule oil release during mixing and compaction was observed and explained by molecular simulation. The oil release due to healing agent inter-diffusion into shell materials was related to temperature and shell concentration, and the interaction between rejuvenator and shell. The major premature failure and content-release for polymeric capsules took place during mixing and compaction at high temperature (160 °C) instead of intermediate temperature (25 °C) due to high thermal movement.
3. The study of interdiffusion and composite mechanical behavior provided insights for capsule design. To prevent premature oil release and ensure the healing efficiency, rejuvenators C and E required 30%–40% calcium alginate, while rejuvenator A needed 40%–60% calcium alginate. This related well to the compositions of the rejuvenators, which indicated that the lower viscosity rejuvenator requires more capsule shell cover to prevent loss during construction.
4. MSD was not a good diffusion indicator for an inter-diffusion system involving two or three layers, because MSD depended on both fraction concentration and fraction's polarity. However, MSD slope could be utilized to understand the contribution of each fraction to rejuvenator diffusion behavior and locate the critical SARA fractions in each capsule. Healing agent A was more easily released than C and E, because of the high saturate content as indicated by MSD.
5. The FAM healing test combined with oil release rate was able to differentiate capsule healing capacities. The healing capacity ranking provided by simulation was validated by FAM healing tests, but the simulation might overestimate the healing capacity by up to 20% due to the limited time and space scales.
6. The healing process included wetting, diffusion, and entanglement. MD provided an understanding of the three mechanisms respectively and determined the effect of rejuvenators and shell thickness. Rejuvenators with more saturates and aromatics might diffuse into openings faster than those comprised of resins and asphaltenes, while rejuvenators with high concentration of asphaltenes could restore more strength than others. Therefore, proper capsule design not only reduced oil release during mixing and compaction but also improved healing efficiency.
7. Fracture and healing simulation in MD confirmed that around 40% shell materials generally prevented the capsule from breaking and led to around 50% reduction of healing index observed from FAM testing. However, high dose shell materials would be desired for local high stress regions. Therefore, multiple designs of capsules could be helpful for healing mixes with complex stress states due to the composite nature of asphalt and aggregates.

8. Future study

This study built a framework for designing capsules from experiments and molecular dynamics simulations and emphasized the potential of predicting thermodynamic and mechanical behaviors. However, more research about the response of capsules to different damage levels could be performed in the future. Also, other mechanical failure cases, such as shear and compression, could be simulated for more realistic engineering of capsules.

This study highlighted the impact of compositional differences among rejuvenators, the molecular weight of structural components, and variations in shell thickness through simulations, demonstrating their influence on capsule strength. However, given the complexities in the relationship between healing agent viscosity and composition, with the rupture strength of the capsules and the composition of the shell material, future experimental research should use experiments to evaluate different shell types. Additionally, future studies should focus on developing larger scale simulation models to more accurately predict the mechanical behavior of capsules.

Future research could incorporate cracking models using the finite element method, to better account for complex stress–strain behaviors and crack propagation paths. It should also explore optimized capsule designs using these models for improved healing efficiency and validate simulation results under real-world macro-scale conditions for improving their practical application capabilities.

CRediT authorship contribution statement

Yujia Lu: Writing – review & editing, Writing – original draft, Methodology, Investigation, Formal analysis, Data curation, Conceptualization. **Bingyan Cui:** Writing – review & editing, Writing – original draft, Investigation, Formal analysis, Data curation. **Hao Wang:** Writing – review & editing, Writing – original draft, Supervision, Methodology, Formal analysis. **Ramez Hajj:** Writing – review & editing, Writing – original draft, Project administration, Methodology, Investigation, Funding acquisition, Formal analysis, Conceptualization.

Declaration of competing interest

The authors declare that they have no known competing financial interests or personal relationships that could have appeared to influence the work reported in this paper.

Data availability

Data will be made available on request.

Acknowledgments

The authors thank the Smart Transportation Infrastructure Initiative (STII) at the University of Illinois, United States for funding this study. The authors would also like to thank Jacob Doehring and Nishant Garg from the University of Illinois for helping with capsule fabrication and ESEM figures. Finally, the authors would like to thank undergraduate research assistant Lucas Zhou for his help in capsule fabrication.

References

[1] M. Alae, L. Xu, Z. Cao, X. Xu, F. Xiao, Fatigue and intermediate-temperature cracking performance of rejuvenated recycled asphalt binders and mixtures: A review, J. Clean. Prod. (2022) 135587.

[2] C. Liu, S. Lv, X. Peng, J. Zheng, M. Yu, Analysis and comparison of different impacts of aging and loading frequency on fatigue characterization of asphalt concrete, J. Mater. Civ. Eng. 32 (9) (2020) 04020240.

[3] B.A. Williams, J.R. Willis, J. Shacat, Asphalt Pavement Industry Survey on Recycled Materials and Warm-Mix Asphalt Usage: 2019, Technical Report, National Asphalt Pavement Association (NAPA), 2020.

[4] S. Ren, X. Liu, P. Lin, S. Erkens, Y. Xiao, Chemo-physical characterization and molecular dynamics simulation of long-term aging behaviors of bitumen, Constr. Build. Mater. 302 (2021) 124437.

[5] R.L. Lytton, J. Uzan, E.G. Fernando, R. Roque, D. Hiltunen, S.M. Stoffels, Development and Validation of Performance Prediction Models and Specifications for Asphalt Binders and Paving Mixes, Vol. 357, Strategic Highway Research Program Washington, DC, 1993.

[6] Y.R. Kim, H.-J. Lee, D.N. Little, Fatigue characterization of asphalt concrete using viscoelasticity and continuum damage theory (with discussion), J. Assoc. Asph. Paving Technol. 66 (1997).

[7] R. Wool, Material damage in polymers, in: Proceedings of NSF Workshop on a Continuum Mechanics Approach to Damage and Life Prediction, Kentucky, 1980, pp. 28–35.

[8] G. Xu, H. Wang, Molecular dynamics study of oxidative aging effect on asphalt binder properties, Fuel 188 (2017) 1–10.

[9] P. Wan, S. Wu, Q. Liu, H. Wang, X. Gong, Z. Zhao, S. Xu, J. Jiang, L. Fan, L. Tu, Extrinsic self-healing asphalt materials: A mini review, J. Clean. Prod. 425 (2023) 138910.

[10] B. Asadi, N. Tabatabaee, Alteration of initial and residual healing potential of asphalt binders due to aging, rejuvenation, and polymer modification, Road Mater. Pavement Des. 23 (2) (2022) 287–307.

[11] J. Cui, X. Li, Z. Pei, Y. Pei, A long-term stable and environmental friendly self-healing coating with polyaniline/sodium alginate microcapsule structure for corrosion protection of water-delivery pipelines, Chem. Eng. J. 358 (2019) 379–388.

[12] S. Liu, M. Kang, K. Li, F. Yao, O. Oderinde, G. Fu, L. Xu, Polysaccharide-templated preparation of mechanically-tough, conductive and self-healing hydrogels, Chem. Eng. J. 334 (2018) 2222–2230.

[13] R. Micaelo, T. Al-Mansoori, A. Garcia, Study of the mechanical properties and self-healing ability of asphalt mixture containing calcium-alginate capsules, Constr. Build. Mater. 123 (2016) 734–744.

[14] N. Ruiz-Riancho, T. Saadoon, A. Garcia, R. Hudson-Griffiths, Enhanced self-healing properties in stone mastic asphalt with encapsulated bitumen rejuvenators, in: Proceedings of the RILEM International Symposium on Bituminous Materials: ISBM Lyon 2020 1, Springer, 2022, pp. 711–717.

[15] L. Zhang, I. Hoff, X. Zhang, C. Yang, Investigation of the self-healing and rejuvenating properties of aged asphalt mixture containing multi-cavity Ca-alginate capsules, Constr. Build. Mater. 361 (2022) 129685.

[16] T. Al-Mansoori, J. Norambuena-Contreras, R. Micaelo, A. Garcia, Self-healing of asphalt mastic by the action of polymeric capsules containing rejuvenators, Constr. Build. Mater. 161 (2018) 330–339.

[17] S. Pavaldi, A. Bhasin, D. Little, A method to quantify healing in asphalt composites using continuum damage approach, in: Proceedings 91st Annual Meeting of Transportation Research Board, Washington DC, United States, 2012.

[18] A. Grangeiro de Barros, L.C.d. Figueirêdo Lopes Lucena, Á. García Hernandez, Addition of encapsulated soybean oil and waste cooking oil in asphalt mixtures: effects on mechanical properties and self-healing of fatigue damage, J. Mater. Civ. Eng. 34 (4) (2022) 04022002.

[19] G. Xu, H. Wang, W. Sun, Molecular dynamics study of rejuvenator effect on RAP binder: Diffusion behavior and molecular structure, Constr. Build. Mater. 158 (2018) 1046–1054.

[20] W. Sun, H. Wang, Self-healing of asphalt binder with cohesive failure: Insights from molecular dynamics simulation, Constr. Build. Mater. 262 (2020) 120538.

[21] A. Bhasin, D.N. Little, R. Bommavaram, K. Vasconcelos, A framework to quantify the effect of healing in bituminous materials using material properties, Road Mater. Pavement Des. 9 (sup1) (2008) 219–242.

[22] Y.L. Yaphary, Z. Leng, H. Wang, S. Ren, G. Lu, Characterization of nanoscale cracking at the interface between virgin and aged asphalt binders based on molecular dynamics simulations, Constr. Build. Mater. 335 (2022) 127475.

[23] B. Cui, H. Wang, X. Gu, D. Hu, Study of the inter-diffusion characteristics and cracking resistance of virgin-aged asphalt binders using molecular dynamics simulation, Constr. Build. Mater. 351 (2022) 128968.

[24] S. Ren, X. Liu, Y. Gao, R. Jing, P. Lin, S. Erkens, H. Wang, Molecular dynamics simulation and experimental validation on the interfacial diffusion behaviors of rejuvenators in aged bitumen, Mater. Des. 226 (2023) 111619.

[25] H. Yu, J. Ge, G. Qian, C. Zhang, W. Dai, P. Li, Evaluation on the rejuvenation and diffusion characteristics of waste cooking oil on aged SBS asphalt based on molecular dynamics method, J. Clean. Prod. 406 (2023) 136998.

[26] W. Sun, H. Wang, Molecular dynamics simulation of diffusion coefficients between different types of rejuvenator and aged asphalt binder, Int. J. Pavement Eng. 21 (8) (2020) 966–976.

[27] Á. García, E. Schlangen, M. van de Ven, G. Sierra-Beltrán, Preparation of capsules containing rejuvenators for their use in asphalt concrete, J. Hazard. Mater. 184 (1–3) (2010) 603–611.

[28] A. Garcia, J. Jelfs, C.J. Austin, Internal asphalt mixture rejuvenation using capsules, Constr. Build. Mater. 101 (2015) 309–316.

[29] P. Singhvi, J.J. García Mainieri, H. Ozer, B. Sharma, Rheology-Chemical Based Procedure to Evaluate Additives/modifiers Used in Asphalt Binders for Performance Enhancements: Phase 2, FHWA-ICT-21-015, Illinois Center for Transportation/Illinois Department of Transportation, 2021.

[30] Y.R. Kim, C. Castorena, N.F. Saleh, E. Braswell, M. Elwardany, F.Y. Rad, Long-Term Aging of Asphalt Mixtures for Performance Testing and Prediction: Phase III Results, Project 09-54, Transportation Research Board, 2021.

[31] A. Filonzi, S.K. Lee, W. Ferreira, R. Hajj, A. Bhasin, A micro-extraction method for use with 4 mm plate geometry in the dynamic shear rheometer to evaluate asphalt binder rheology, Constr. Build. Mater. 252 (2020) 119024.

[32] M.L. Williams, R.F. Landel, J.D. Ferry, The temperature dependence of relaxation mechanisms in amorphous polymers and other glass-forming liquids, J. Am. Chem. Soc. 77 (14) (1955) 3701–3707.

[33] P. Karki, R. Li, A. Bhasin, Quantifying overall damage and healing behaviour of asphalt materials using continuum damage approach, Int. J. Pavement Eng. 16 (4) (2015) 350–362.

[34] D. Hu, X. Gu, Q. Dong, L. Lyu, B. Cui, J. Pei, Investigating the bio-rejuvenator effects on aged asphalt through exploring molecular evolution and chemical transformation of asphalt components during oxidative aging and regeneration, J. Clean. Prod. 329 (2021) 129711.

[35] Z. Sun, J. Yi, Y. Huang, D. Feng, C. Guo, Properties of asphalt binder modified by bio-oil derived from waste cooking oil, Constr. Build. Mater. 102 (2016) 496–504.

[36] Y. Zhang, S. Wu, G. Liu, Influence of bio-rejuvenator on the rheological properties of aged asphalt binder, in: Advances in Energy and Environmental Materials: Proceedings of Chinese Materials Conference 2017 18th, Springer, 2018, pp. 717–726.

[37] D.D. Li, M.L. Greenfield, Chemical compositions of improved model asphalt systems for molecular simulations, Fuel 115 (2014) 347–356.

[38] O. Smidsrød, A. Haug, B. Lian, A. Huhtikangas, W. Pearson, V. Meisalo, Properties of poly (1, 4-hexuronates) in the gel state. II. Comparison of gels of different chemical composition, Acta Chem. Scand. 26 (1972) 79–88.

[39] G.O. Aspinall, The Polysaccharides, Academic Press, 2014.

[40] A.P. Thompson, H.M. Aktulga, R. Berger, D.S. Bolintineanu, W.M. Brown, P.S. Crozier, P.J. in't Veld, A. Kohlmeyer, S.G. Moore, T.D. Nguyen, et al., LAMMPS-a flexible simulation tool for particle-based materials modeling at the atomic, meso, and continuum scales, Comput. Phys. Comm. 271 (2022) 108171.

[41] P. Dauber-Osguthorpe, V.A. Roberts, D.J. Osguthorpe, J. Wolff, M. Genest, A.T. Hagler, Structure and energetics of ligand binding to proteins: Escherichia coli dihydrofolate reductase-trimethoprim, a drug-receptor system, Proteins: Struct. Funct. Bioinform. 4 (1) (1988) 31–47.

[42] I. Jeon, J. Lee, T. Lee, T. Yun, S. Yang, In silico simulation study on moisture-and salt water-induced degradation of asphalt concrete mixture, Constr. Build. Mater. 417 (2024) 135229.

[43] H. Zhang, J. Cao, H. Duan, H. Luo, X. Liu, Molecular dynamics insight into the adsorption and distribution of bitumen subfractions on Na-montmorillonite surface, Fuel 310 (2022) 122380.

[44] M. Xu, J. Yi, D. Feng, Y. Huang, Diffusion characteristics of asphalt rejuvenators based on molecular dynamics simulation, Int. J. Pavement Eng. 20 (5) (2019) 615–627.

[45] I.L. Hia, E.-S. Chan, S.-P. Chai, P. Pasbakhsh, A novel repeated self-healing epoxy composite with alginate multicore microcapsules, J. Mater. Chem. A 6 (18) (2018) 8470–8478.

[46] S. Ren, X. Liu, P. Lin, S. Erkens, Y. Gao, Chemical characterizations and molecular dynamics simulations on different rejuvenators for aged bitumen recycling, Fuel 324 (2022) 124550.

[47] C. Li, S. Fan, T. Xu, Method for evaluating compatibility between SBS modifier and asphalt matrix using molecular dynamics models, J. Mater. Civ. Eng. 33 (8) (2021) 04021207.

[48] G.R. Quezada, C. Solar, J.H. Saavedra, K. Petit, F.J. Martin-Martínez, L.E. Arteaga-Pérez, J. Norambuena-Contreras, Operando FTIR-ATR with molecular dynamic simulations to understand the diffusion mechanism of waste tire-derived pyrolytic oil for asphalt self-healing, Fuel 357 (2024) 129834.

[49] Z. Long, X. Tang, N. Guo, Y. Ding, W. Ma, L. You, F. Xu, Atomistic-scale investigation of self-healing mechanism in nano-silica modified asphalt through molecular dynamics simulation, J. Infrastruct. Preserv. Resil. 3 (1) (2022) 1–24.

[50] D. Sun, G. Sun, X. Zhu, F. Ye, J. Xu, Intrinsic temperature sensitive self-healing character of asphalt binders based on molecular dynamics simulations, Fuel 211 (2018) 609–620.

[51] L. He, G. Li, S. Lv, J. Gao, K.J. Kowalski, J. Valentin, A. Alexiadis, Self-healing behavior of asphalt system based on molecular dynamics simulation, Constr. Build. Mater. 254 (2020) 119225.

[52] A. Ghaffari, A. Rahbar-Kelishami, MD simulation and evaluation of the self-diffusion coefficients in aqueous NaCl solutions at different temperatures and concentrations, J. Mol. Liq. 187 (2013) 238–245.

[53] S. Ren, X. Liu, Y. Zhang, P. Lin, P. Apostolidis, S. Erkens, M. Li, J. Xu, Multi-scale characterization of lignin modified bitumen using experimental and molecular dynamics simulation methods, Constr. Build. Mater. 287 (2021) 123058.